

# An analytical model for dynamic radius prediction of a penny-shaped hydraulic fracture at depth

Runhua Feng (✉ [runhua.feng@student.curtin.edu.au](mailto:runhua.feng@student.curtin.edu.au))

Curtin University <https://orcid.org/0000-0003-1722-4265>

Joel Sarout

CSIRO Kensington: CSIRO Australian Resources Research Centre

Jeremie Dautriat

CSIRO Kensington: CSIRO Australian Resources Research Centre

Jiecheng Zhang

Peking University School of Earth and Space Sciences

Hamid Roshan

UNSW: University of New South Wales

Reza Rezaee

Curtin University - Perth Bentley Campus: Curtin University

mohammad sarmadivaleh

Curtin University Bentley Campus: Curtin University

---

## Research Article

**Keywords:** Dynamic radius prediction, Penny-shaped hydraulic fracture, Linear Elasticity, Poiseuille's law, Self-similar propagation

**Posted Date:** April 14th, 2022

**DOI:** <https://doi.org/10.21203/rs.3.rs-1525036/v1>

**License:**  This work is licensed under a Creative Commons Attribution 4.0 International License.

[Read Full License](#)

---

## **An analytical model for dynamic radius prediction of a penny-shaped hydraulic fracture at depth**

Runhua Feng<sup>1\*</sup>, Joel Sarout<sup>2</sup>, Jeremie Dautriat<sup>2</sup>, Jiecheng Zhang<sup>3</sup>, Hamid Roshan<sup>4</sup>, Reza Rezaee<sup>1</sup>, Mohammad Sarmadivaleh<sup>1</sup>

<sup>1</sup>School of WASM: Minerals, Energy and Chemical Engineering, Curtin University, 26 Dick Perry Ave, Kensington, WA 6151 Australia

<sup>2</sup>CSIRO Energy, Perth, WA 6151, Australia

<sup>3</sup>Beijing International Center for Gas Hydrate, School of Earth and Space Sciences, Peking University, Beijing 100871, China

<sup>4</sup>School of Minerals and Energy Resources Engineering, UNSW AUSTRALIA, Kensington, Sydney 2052, Australia

\*Corresponding author:

E-mail address: runhua.feng@student.curtin.edu.au (R.Feng)

### **Highlights:**

- Two analytical models are developed to predict the time evolution of the radius of a penny-shaped hydraulic fracture
- The linear elastic fracture model is suitable only for limited conditions, i.e., non-viscous dominated propagation regimes with negligible fluid lag and a stable fracture propagation
- The self-similar fracture growth model based on Poiseuille's law, scaling and dimensional analysis takes advantage of a fast reconstruction of the dynamic radius of finite hydraulic fracture problems under more realistic conditions, i.e., multiscale propagation regimes, cohesive effects, stable and unstable propagation in different geomaterials.

## Abstract

Hydraulic fracturing is a coupled multi-physics and scale-dependent process requiring an extensive numerical-laboratory appraisal prior to a field trial. Developing a robust model of hydraulic fracture propagation requires knowledge of the time evolution of the fracture's geometrical attributes, e.g., width/aperture and length/radius. However, it is inherently challenging to directly measure even the simplest fracture attribute (i.e., dynamic radius) within the rock sample subjected to *in-situ* stress conditions. In this study, two analytical models are developed to predict the time evolution of the radius of a penny-shaped hydraulic fracture. In the first model ( $R_E$ ), the incremental fracture propagation of an infinite hydraulic fracture is described using linear elasticity, modified to incorporate a realistic distribution of internal fluid pressure using a Taylor series. The second model ( $R_d$ ) predicts the fracture opening and internal pressure gradient using Poiseuille's law and assuming a self-similar propagation. Scaling and dimensional analysis are used to define propagation regimes; non-linear hydro-mechanical coupling is accounted for in the near-tip region (process- or cohesive-zone). Finally, the two analytical models are compared against published experimental data. Our results show that the radius prediction based on linear elasticity ( $R_E$ ) is suitable only for limited conditions, i.e., non-viscous dominated propagation regimes with negligible fluid lag and a stable fracture propagation. On the other hand, the  $R_d$  model takes advantage of a fast reconstruction of the dynamic radius of finite hydraulic fracture problems under more realistic conditions, i.e., including multiscale propagation regimes, cohesive effects, stable and unstable propagation in different geomaterials.

**Keywords:** Dynamic radius prediction; Penny-shaped hydraulic fracture; Linear Elasticity; Poiseuille's law; Self-similar propagation

## 1. Introduction

Fluid-driven fracture propagation has been extensively studied for application to subsurface reservoir stimulation operations (Bunger 2005; Adachi et al. 2007; Sarmadivaleh 2012; Lecampion et al. 2017; Garagash 2019; Feng et al. 2020; Zeng et al. 2020; Huang and Chen 2021), geothermal energy extraction (Legarth et al. 2005; Shao et al. 2015), CO<sub>2</sub> geo-sequestration (Papanastasiou et al. 2016), control of fluid-induced seismicity (Amitrano 2003; Shapiro 2015), and modelling of magma migration (Weinberg and Regenauer-Lieb 2010). The

underlying hydro-mechanical interactions taking place at depth are governed by the coupling between fluid flow and rock deformation under prescribed *in-situ* stress conditions.

Early investigations of crack propagation in solids were based on mathematical solutions of elasticity, i.e., solving integral equations (England and Green 1963; Green and Zerna 1992), or using the Fourier transform (Sneddon 1946; Sneddon 1995). In the initial attempts, mathematical solutions were proposed for the propagation of a Griffith fracture in plane strain (Sneddon and Elliot 1946), and for the propagation of a penny-shaped fracture in three dimensions (Sneddon 1946).

Later, these models were enriched to account for fluid flow, fluid mass balance and fracture geometry, and applied to hydraulic fracturing problems, e.g., (i) Perkins and Kern (1961) and Nordgren (1972) developed the so-called PKN model for the propagation in the horizontal direction of a vertical fracture with an elliptical cross-section, assuming a constant fracture height much smaller than fracture length, and a one-dimensional fluid flow within the fracture; (ii) Zheltov (1955) and Geertsma and De Klerk (1969) developed the so-called KGD model for the propagation in the horizontal direction of a vertical fracture with a rectangular cross-section, assuming a constant fracture height much larger than the fracture length, and a one-dimensional fluid flow within the fracture; and (iii) Abé et al. (1976) and Advani et al. (1987) developed a propagation model for a two-dimensional penny-shaped hydraulic fracture, accounting for two-dimensional fluid flow within it (**Fig.1a**).

To remain mathematically tractable, these analytical models are generally based on simplifying assumptions corresponding to asymptotic regimes that can be relevant in specific conditions. In practice though, they only offer approximate solutions to actual, more complex problems in the field, e.g., heterogeneity of the rock formation or fluid leak-off within the fracture. In fact, hydromechanical coupling and the impact of the boundary conditions (far field stress) will lead to non-linear fracture propagation locally, which must be captured in order to achieve robust and accurate predictions for a specific application.

To address the inherent limitations of analytical models, numerical simulations of fracture propagation in pseudo-3D were introduced in the early 70s (Simonson et al. 1978; Fung et al. 1987), followed by more accurate but costly planar-3D (PL3D) models (Clifton and Abou-Sayed 1981; Vandamme and Curran 1989; Advani et al. 1990; Clifton and Wang 1991; Naceur et al. 1990). Recently, Lecampion and Desroches (2015) presented a PL3D model for the initiation and propagation of a radial fracture based on an implicit time-stepping scheme and involving the Displacement Discontinuity Method (DDM) (Lecampion and Detournay 2007). Notably, this model captures the initiation and early-time propagation of the fracture, when

nonlinearity dominates. Alternatively, the time and scale integration of multiple tip asymptotic solutions to predict hydraulic fracture propagation leads to a good agreement with experimental data for homogeneous and brittle materials such as Polymethyl Methacrylate (PMMA), or synthetic cement/sand samples (Garagash and Detournay 2000; Savitski and Detournay 2002; Lecampion et al. 2017; Lecampion and Detournay 2007; Bungler and Detournay 2007). However, this approach requires to iteratively track the front of the propagating fracture and update the system of equations, which is computationally costly in practice. In addition, the application of the DDM is restricted to homogenous and linear elastic solids (Lecampion and Desroches 2015). For heterogeneous rocks with non-local deformation around the fracture tip (process zone) a discrepancy exists between model predictions and experimental observations, typically in terms of wellbore pressure and fracture width (Lecampion et al. 2017). Note also that computational costs are aggravated when modelling heterogeneous or anisotropic reservoirs.

Linear hydraulic fracture mechanics (LHFM) incorporates linear elastic fracture mechanics (LEFM) and Poiseuille's flow law. This approach is widely used to model the growth of a hydraulic fracture in homogeneous and brittle materials such as PMMA or glass (Bunger and Detournay 2008; Liu 2021). However, the nonlinearity induced by the deformation and energy dissipation taking place in the cohesive (process) zone, and by fluid flow near the tip region within quasi-brittle materials (e.g., sedimentary rock) are often neglected (Liu 2021). Earlier studies show that the LHFM approach is suitable for low ratio of confining to cohesive stress ( $\sigma_o/\sigma_c$ ). Significant deviations from LHFM predictions are observed in laboratory or field applications when the dimensionless ratio  $\sigma_o/\sigma_c$  becomes large (Adachi et al. 2007; Garagash 2019). This may explain the discrepancy observed between numerical simulation results and experimental observations for heterogeneous rocks subjected to realistic triaxial stress fields (De Pater et al. 1994b; van Dam et al. 2000; Lecampion et al. 2017). For example, Poiseuille's cubic flow law is well accepted for modelling the laminar flow of highly viscous fluids such as magma within fractures, where the process zone is embedded in the fluid lag zone (**Fig.1b**). However, for a low-viscosity fracturing fluid (e.g., slick water or gel), the lag zone is usually embedded in the process zone (**Fig.1c**), where the cubic flow law is no longer valid (Garagash 2019). Therefore, for quasi-brittle materials, the determination of the fluid lag and cohesive zone adjacent to the crack tip are necessary for validating the use of Poiseuille's cubic flow law in modelling hydraulic fracturing.

Simultaneous measurement of the borehole pressure (BHP), fracture radius ( $R$ ), and width/aperture ( $w$ ) of a hydraulic fracture under true triaxial stress condition (TTSC) are scarce

in the literature (De Pater et al. (1994b); Lhomme (2005)). In the laboratory, the width of hydraulic fracture can be estimated by measuring the bulk deformation of the rock sample with Linear Variable Differential Transformers (LVDT) attached to its faces, or internal LVDTs located within the wellbore. However, tracking the evolution of the fracture's radius is technically more challenging. Such radius estimations were traditionally performed on samples of transparent material with a high-speed camera (Bunger 2005), or using active and/or passive ultrasonic monitoring (De Pater et al. 1994b; Lhomme 2005; Nabipour 2013). To overcome the aforementioned mathematical, numerical, or experimental challenges for tracking the extent of a hydraulic fracture, it is essential to develop a robust model using the less and most reliable input data, for application to the widest range of underground stimulation projects. Here, we adopt the theory of linear elasticity and incorporate a realistic distribution of fluid pressure within the fracture obtained by Taylor expansion of the theoretical fluid pressure distribution expected in an elliptical fracture. This is then used to compute the displacement induced by the fracture and invert for the dynamic radius  $R_E$ . On the other hand, we develop a new analytical model for the dynamic evolution of the fracture radius  $R_d$  for a finite and radial hydraulic fracture (**Fig.1a**). For this  $R_d$  model, and based on dimensional analysis, we discuss the possible propagation regimes for various near-tip conditions (i.e., cohesive zone, fluid lag). The two analytical models  $R_E$  and  $R_d$  are then verified using literature data (i.e., seven different materials: cement/sand, Colton and Felser sandstones, and PMMA). Finally, the results and recommendations of the  $R_d$  model are discussed. **Table 1** compares the characteristics of the two models as defined in the literature and in the present article.

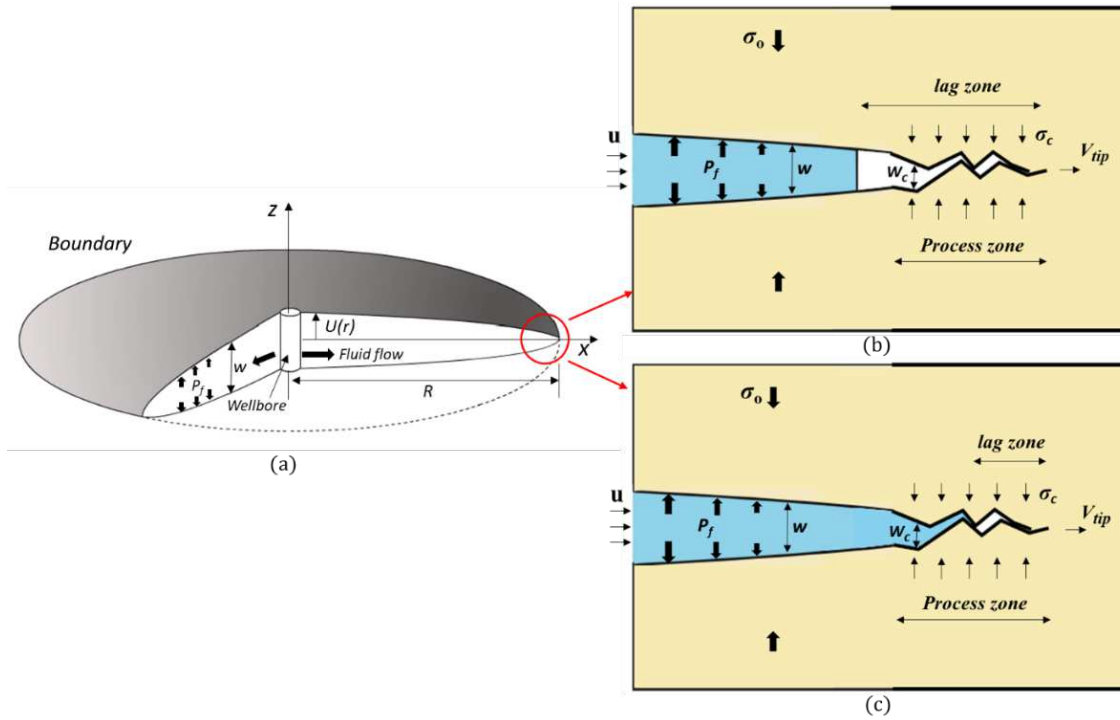


**Fig.1** Schematic of penny-shaped hydraulic fracture **a)** 3D geometry of propagation adapted from Savitski and Detournay (2002) and Valkó and Economides (1995), **b)** the near-tip region modelled as Poiseuille flow with significant lag in a semi-infinite crack (image modified from Garagash (2015)) and **c)** the near-tip region modelled as “rough” channel flow with limited lag zone in a semi-infinite crack (image modified from Garagash (2019)).

**Table 1.** Radius prediction of penny-shaped hydraulic fracture: Comparison between existing methods and our analytical models

	Reference	Assumption	Early-time initiation	Fluid lag	Cohesive zone
Analytical solutions	Abé et al. 1976; Advani et al. 1987	Homogeneous, linear elastic medium			
Numerical work	Lecampion and Desroches (2015); Lecampion et al (2017)	Homogeneous isotropic medium	✓	✓	
Experimental measurement	Lhomme (2005); Nabipour (2013)	N/A	✓		
Dynamic radius model $R_E$ (analytical)	Sneddon (1946); Valkó and Economides (1995) Modified in this paper	linear elastic medium	✓		
Dynamic radius model $R_d$ (analytical)	Defined in this paper	Self-similar propagation	✓	✓	✓

## 2. Theory

### 2.1 Elastic fracture growth model ( $R_E$ )

Linear elasticity is widely applied for static equilibrium of solids (Green and Zerna 1992; Valkó and Economides 1995). For the propagation of a penny-shaped fracture (**Fig.1a**), borehole pressure (BHP) is a function of mechanical properties (Young's modulus  $E$  and Poisson's ratio  $\nu$ ), fracture dimensions  $R$  and  $w$ , and time  $t$ , i.e.,  $BHP = f(w, R, E, \nu, t)$ . The propagation of hydraulic fractures can be described by linear elasticity using the Fourier transform (Sneddon 1995). Solving the initial-boundary value problem for a penny-shaped fracture entails constructing an auxiliary function  $g(\xi)$  (Green and Zerna 1992; Sneddon 1995; Valkó and Economides 1995), i.e.,

$$g(\xi) = \frac{2}{\pi} \int_0^\xi \frac{rP(r)dr}{(\xi^2 - r^2)^{\frac{1}{2}}}, \text{ with } 0 < \xi < R, \quad (1)$$

where  $\xi$  is a dummy length variable;  $g(\xi)$  possesses the dimension of a fluid pressure  $P$ ;  $r$  is the apparent radius, and  $R$  is the maximum radius of the finite fracture. Considering **Eq. (1)**, the normal displacement of any point on the upper part of the fracture disk reads

$$U_z(r, 0) = \frac{2}{E'} \int_r^R \frac{\xi g(\xi) d\xi}{(\xi^2 - r^2)^{\frac{1}{2}}}, \text{ with } 0 \leq r \leq R. \quad (2)$$

where  $E'$  is the plane strain modulus.

For a uniform fluid pressure within the fracture,  $P(\xi) = P_0$ , and the auxiliary function (**Eq.1**) reduces to

$$g(\xi) = P_0 \xi. \quad (3)$$

Integration over the fracture's radius  $r$  yields the fracture's aperture  $w = 2 U_z(r)$ , i.e.,

$$w(r) = \frac{8}{\pi E} P_0 \sqrt{R^2 - r^2}. \quad (4)$$

However, fluid pressure is not uniform in a real hydraulic fracture, and more complex fluid pressure distributions can be simplified using a polynomial Taylor expansion in terms of the small variable  $\xi$ , i.e.,

$$P(\xi) = P_0 + \frac{P_1}{1!} \xi + \frac{P_2}{2!} \xi^2 + \frac{P_3}{3!} \xi^3 + \dots \quad (5)$$

where  $P_0$  is the initial fluid pressure when wellbore breakdown occurs,  $P_1$ ,  $P_2$ , and  $P_3$  are the primary, secondary, and ternary pressure gradients (i.e.,  $P_1 = \frac{\partial p}{\partial r}$ ,  $P_2 = \frac{\partial p^2}{\partial^2 r}$ ,  $P_3 = \frac{\partial p^3}{\partial^3 r}$ ).

Using **Eq. (5)**, the auxiliary function  $g(\xi)$  (**Eq.1**) can be rewritten as:

$$g(\xi) = \frac{2}{\pi} (P_0 + \frac{P_1}{1!} \xi + \frac{P_2}{2!} \xi^2 + \frac{P_3}{3!} \xi^3 + \dots) \quad (6)$$

Substitution of **Eq. (6)** into **Eq. (2)** and integration yields the width of the pressurized fracture  $w(r)$  as

$$w(r) = \frac{2}{\pi E} * \left\{ 4 * P_0 * (R^2 - r^2)^{0.5} + P_1 * \left[ R * (R^2 - r^2)^{0.5} + r^2 * \ln \left( \frac{R + (R^2 - r^2)^{0.5}}{r} \right) \right] + \frac{1}{6} P_2 * (R^2 + 2r^2) * (R^2 - r^2)^{0.5} + \frac{3}{48} \frac{\partial p^3}{\partial^3 r} \left[ \left( \frac{2}{3} * R^3 + R * r^2 \right) * (R^2 - r^2)^{0.5} + r^4 * \ln \left( \frac{R + (R^2 - r^2)^{0.5}}{r} \right) \right] + \dots \right\} \quad (7)$$

where the magnitude of the terms with higher order ( $P_4, P_5 \dots P_n$ ) are small enough to be negligible compared to the first three terms in **Eq. (7)**. The secondary pressure gradient ( $P_2$ ) must be accounted for to compensate for the positive primary pressure gradient ( $P_1$ ); therefore, **Eq. (7)** reduces to

$$w(r) = \frac{2}{\pi E} * \left\{ 4 * P_0 * (R^2 - r^2)^{0.5} + P_1 * \left[ R * (R^2 - r^2)^{0.5} + r^2 * \ln \left( \frac{R + (R^2 - r^2)^{0.5}}{r} \right) \right] + \frac{1}{6} P_2 * (R^2 + 2r^2) * (R^2 - r^2)^{0.5} \right\} \quad (8)$$

For an elliptical cross-section of the fracture as defined in **Fig.1a**, the maximum width occurs at the wellbore ( $r = 0$ ); therefore **Eq. (8)** reduces to

$$w_{max}(r_0) = \frac{2}{\pi E} * \left\{ 4 * P_0 * R + P_1 * R^2 + \frac{1}{6} P_2 * R^3 \right\}, \text{ with } r = 0 \quad (9)$$

Correspondingly, the minimum width will occur at tip, where  $r = R$ ; **Eq.8** then reduces to

$$w_{min}(r_R) = 0, \text{ with } r = R \quad (10)$$

## 2.2 Self-similar fracture growth model ( $R_d$ )

Poiseuille's law is used to describe the flow of Newtonian fluids driven by fluid pressure within a penny shaped fracture (Batchelor and Batchelor 2000; Lecampion et al. 2017)

$$q = - \frac{w^3}{12 \mu_f} \frac{\partial p_f}{\partial r} \quad (11)$$

where  $q$  is the flow rate per unit perimeter of the fracture;  $w$  is the width/opening of the fracture;  $\mu_f$  is the viscosity of the fluid;  $P_f$  is the fluid pressure; and  $r$  is the fracture radius. Assuming a self-similar (homothetic) hydraulic fracture growth for **Eq. (11)** (see **Fig.2**), and considering the fluid velocity of  $u = \frac{dr}{dt}$  within the fracture, the flow rate per unit fracture perimeter,  $q = wu$ , and the fluid pressure gradient can be related by its partial derivative  $\frac{\partial p_f}{\partial r} = \frac{\partial p_f}{\partial t} \frac{dt}{dr}$  (assuming all other variables are at quasi-static conditions). Therefore, fluid velocity can be rewritten as

$$\frac{dr}{dt} = w \sqrt{-\frac{1}{12\mu_f} \frac{\partial p_f}{\partial t}}. \quad (12)$$

Reported experimental literature suggests that the geometry of laboratory-scale hydraulic fracture tests conducted on low permeability rocks are approximately penny-shaped transverse or longitudinal fractures (Bunger 2005; Lhomme 2005; Rodriguez and Stanchits 2017; Sarmadivaleh 2012). In this context, the cumulated volume of an incompressible fluid injected into the fracture with time at a distance of  $R$  from the wellbore (end of propagation) is  $V_T = 2\pi \int_0^R r w dr = \pi w R^2$ . Similarly, the cumulated volume at time  $t$ , when the fracture reaches a radius  $r(t)$  during propagation, is related to the average (constant) flow rate  $Q_{in}$  by

$$V(t) = 2\pi \int_0^r r w dr = \pi w r^2 = w A_r = Q_{in} t, \quad (13)$$

where  $A_r = \pi r^2$  is the fracture's surface area at time  $t$ . Noting that  $\frac{dA_r}{dt} = 2\pi r \frac{dr}{dt}$ , and using

**Eq. (12)** yields

$$\frac{dA_r}{dt} = 2\pi r \sqrt{-\frac{w^2}{12\mu_f} \frac{\partial p_f}{\partial t}}. \quad (14)$$

For a self-similar (homothetic) propagation of the penny-shaped fracture, and for a small enough incremental increase in fracture surface area  $(\Delta A_r)_m$  per time increment  $\Delta t_m$ , **Eq. (14)** can be discretised as

$$\frac{(\Delta A_r)_m}{\Delta t_m} \cong 2\pi r_m \sqrt{-\frac{w_m^2}{12\mu_f} \left(\frac{\Delta p_f}{\Delta t}\right)_m}, \quad 1 \leq m \leq N \quad (15)$$

where  $2\pi r_m$  represents the circumference of the self-similarly moving boundary of the growing penny-shaped fracture (**Fig.2**). Note that  $(\Delta A_r)_m$  is again proportional to  $\sqrt{-\frac{w_m^2}{12\mu_f} \left(\frac{\Delta p_f}{\Delta t}\right)_m}$ , i.e.,

$$(\Delta A_r)_m \propto \sqrt{-\frac{w_m^2}{12\mu_f} \left(\frac{\Delta p_f}{\Delta t}\right)_m}. \text{ Introducing the factor of proportionality } \lambda_m, \text{ and the intercept,}$$

$B_m$  (See **Section 3.3** for validation) leads to:

$$(\Delta A_r)_m = \lambda_m \sqrt{-\frac{w_m^2}{12\mu_f} \left(\frac{\Delta p_f}{\Delta t}\right)_m} + B_m \quad (16)$$

Let  $A_T$  be the total (maximum) fractured area, up to the boundary of the sample where  $r = R$ . Using **Eq.(16)** to define a dimensionless term, the dynamically-evolving surface ratio  $(\Delta A_r)_m/A_T$ , leads to

$$\frac{(\Delta A_r)_m}{A_T} = \frac{\lambda_m \sqrt{-\frac{w_m^2}{12\mu_f} \left(\frac{\Delta p_f}{\Delta t}\right)_m} + B_m}{\sum_{i=1}^N \left( \lambda_i \sqrt{-\frac{w_i^2}{12\mu_f} \left(\frac{\Delta p_f}{\Delta t}\right)_i} + B_i \right)}, \quad \text{with } 1 \leq i \leq N \text{ and } 1 \leq m \leq N \quad (17)$$

where the indices  $i$  and  $m$  reflect the time steps between the nucleation ( $i = m = 1$ ) and the end of propagation ( $i = m = N$ ) of the hydraulic fracture, i.e., when it reaches the rock sample's boundary. For sake of simplicity, we further assume a steady fracture growth, implying that  $\lambda_m = \lambda$  is constant during propagation. Fitting **Eq.(16)** to the fracture growth data published in the literature, we can estimate  $\lambda_m = \lambda$  and  $B_\kappa$  (see details in **Section 3.3**). It is found that  $B_m$  is negligible, i.e.,  $B_m \ll (\Delta A_r)_m$ , and **Eq.(17)** can be approximated by

$$(\Delta A_r)_m \cong \frac{A_T \sqrt{\frac{w_m^2}{12\mu_f} \left(\frac{\Delta p_f}{\Delta t}\right)_m}}{\sum_{i=1}^N \sqrt{\frac{w_i^2}{12\mu_f} \left(\frac{\Delta p_f}{\Delta t}\right)_i}}, \quad \text{with } 1 \leq i \leq N \text{ and } 1 \leq m \leq N \quad (18)$$

Therefore, the cumulative increase in fracture area with time,  $A_d$  between fracture nucleation,  $\kappa = 1$  and a later time step,  $m = n$  (where  $n \leq N$ ) reads (see **Fig.2**)

$$A_d \cong \sum_{\kappa=1}^n (\Delta A_r)_m = A_T \frac{\sum_{m=1}^n \left( \sqrt{\frac{w_m^2}{12\mu_f} \left(\frac{\Delta p_f}{\Delta t}\right)_m} \right)}{\sum_{i=1}^N \left( \sqrt{\frac{w_i^2}{12\mu_f} \left(\frac{\Delta p_f}{\Delta t}\right)_i} \right)}, \quad \text{with } 1 \leq i \leq N \text{ and } 1 \leq m \leq n \leq N \quad (19)$$

It can be seen from **Eq.(12)** that  $w$  is proportional to  $\frac{dr}{dt}$ , ( $w \propto \frac{dr}{dt}$ ) when the energy dissipation during propagation is dominated by viscous fluid flow, i.e., viscosity-dominated regime (Garagash 2019; Peck et al. 2018). However, cohesive-zone effects can dissipate significant amounts of energy in the near-tip region. This type of dissipation is related to the fluid lag within the process zone, which has been experimentally observed by Lhomme (2005) and theoretically proved by Garagash (2019) and Liu and Lecampion (2021). When energy dissipation is dominated by cohesive-zone or near-tip effects, (i) the fracture opening,  $w$  becomes proportional to  $\left(\frac{dr}{dt}\right)^{\frac{3}{2}}$ , ( $w \propto \left(\frac{dr}{dt}\right)^{\frac{3}{2}}$ ), and (ii) the coefficient of proportionality remains the same as for the viscosity-dominated regime, i.e.,  $\sqrt{-\frac{1}{12\mu_f} \frac{\partial p_f}{\partial t}}$  (see details in Garagash and Detournay (2000) or Garagash (2019)). In this case, **Eq. (12)** becomes

$$\frac{dr}{dt} \propto w^{\frac{2}{3}} \sqrt[3]{-\frac{1}{12\mu_f} \frac{\partial p_f}{\partial t}}, \quad (20)$$

and **Eq.(19)** is replaced by

$$A_d \cong A_T \frac{\sum_{k=1}^n \left( \sqrt[3]{\frac{w_m^2}{12\mu_f} \left( \frac{\Delta p_f}{\Delta t} \right)_m} \right)}{\sum_{i=1}^N \left( \sqrt[3]{\frac{w_i^2}{12\mu_f} \left( \frac{\Delta p_f}{\Delta t} \right)_i} \right)}, \quad \text{with } 1 \leq i \leq N \text{ and } 1 \leq m \leq n \leq N \quad (21)$$

**Eqs. (19) and (21)** are used to model the evolution of the dynamic fracturing area (see **Section 3.3** for details). The equivalent dynamic radius ( $R_d$ ) is defined as

$$R_d = \sqrt{\frac{A_d}{\pi}} \quad (22)$$

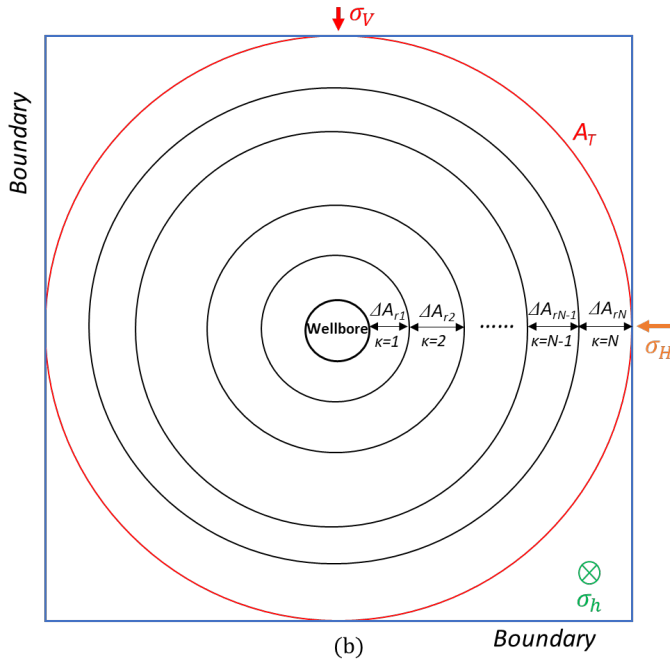


**Fig.2** 2D schematic of the self-similar evolution of the radial fracture, outlining the dynamic fracture surface area  $A_d$ .

### 2.3 Fracture propagation regimes

A dimensionless group, i.e., time scale ( $t_{om}$ ,  $t_{mk}$ ), dimensionless toughness ( $k$ ), and the time scale ratios ( $\chi$ ,  $\Psi$ ) have been introduced to analyse fracture propagation regimes (Bunger and Detournay 2007; Detournay 2004; Garagash 2006; Lecampion et al. 2017; Lhomme 2005; Savitski and Detournay 2002). Three scaled material parameters were defined by dimensional analysis

$$K' = \left( \frac{32}{\pi} \right)^{\frac{1}{2}} K_{IC}, E' = \frac{E}{1-\nu^2} K_{IC}, \mu' = 12\mu \quad (23)$$

where  $K_{IC}$  is the fracture toughness,  $E$  is Young's Modulus,  $\nu$  is Poisson's ratio, and  $\mu$  is the viscosity of the fluid. For a constant fluid injection rate  $Q_o$ , a time scale  $t_{mk}$  is defined as the

time required for fracture propagation to evolve from a viscosity-dominated regime at early times to a toughness-dominated one at larger times

$$t_{mk} = \left( \frac{\mu'^5 Q_0^3 E'^{13}}{K'^{18}} \right)^{\frac{1}{2}}, \quad (24)$$

and a dimensionless toughness  $k$  is introduced for discriminating between the two propagation regimes, i.e.,

$$k = K' \left( \frac{t^2}{\mu'^5 Q_0^3 E'^{13}} \right)^{\frac{1}{18}} \quad (25)$$

A time scale ratio  $\chi$  is also introduced to capture the transition from the early-time fracture initiation driven by the compressibility of the injection system, to the large-time steady propagation at a constant injection rate  $Q_0$  (Lecampion et al. 2017), i.e.,

$$\chi = \frac{E'^4 Q_0^{3/2} \mu'^{3/2}}{K'^6 U^{1/2}}, \quad (26)$$

where  $U$  is the compliance of the injection system, i.e., combined compressibility of the fluid, the pumping system. Another time scale ratio  $t_{om}$  is also introduced for the toughness-dominated regime driven by fluid lag, i.e.,

$$t_{om} = \frac{E'^2 \mu'}{\sigma_0^3}, \quad (27)$$

where  $\sigma_0$  is the confining stress applied at the fracture's surface. A third time scale ratio  $\Psi$  is introduced for the transition from the toughness-dominated regime driven by fluid lag, to the large-time propagation regime (Lecampion et al. 2017)

$$\Psi = \frac{t_{mk}}{t_{om}} = \left( \frac{E'^{3/2} Q_0^{1/2} \mu'^{1/2} \sigma_0}{K'^3} \right)^3. \quad (28)$$

Garagash (2015), Garagash (2019), and Liu and Lecampion (2021) showed that (see summary in **Table 2**)

- (i) If  $k < 1$  and  $\Psi \gg 1$ , the fracture propagates in a viscosity-dominated regime with significant fluid lag (**Fig.1b**); in this situation Poiseuille's flow law is valid, and **Eqs. (19) and (22)** can be used to estimate  $A_d$  and  $R_d$ , respectively;
- (ii) If  $1 \leq k \leq 4$  and  $\Psi \ll 1$ , the fracturing fluid invades the process zone (**Fig.1c**), resulting in local turbulent fluid flow and significant deviation from Poiseuille's flow law; in this situation **Eq. (21)** can be used to estimate  $A_d$ ;
- (iii) If  $1 \leq k \leq 4$  and  $\Psi \gg 1$ , the ratio of confining stress ( $\sigma_0$ ) to cohesive stress ( $\sigma_c$ ),  $\sigma_0/\sigma_c$ , becomes critical. A large  $\sigma_0/\sigma_c$  ratio accelerates the penetration of the fluid into the cohesive zone, and is modelled as inversely proportional to the size of the

fluid lag zone (Garagash 2019; Liu and Lecampion 2021). Their numerical results (Liu and Lecampion 2021) suggest that for a dimensionless toughness  $k = 2$ , the fluid fraction  $\zeta$  ranges from 0.85 to 0.98 when  $\sigma_o/\sigma_c$  ranges from 1 to 10. In this situation, the ratio between the size of the fluid lag and that of the cohesive zone is relatively small. Therefore, we argue that this case is similar to case **(ii)**, and **Eqn (21)** can also be used to estimate  $A_d$ ;

- (iv)** If  $k > 4$ , a strongly toughness-dominated propagation regime, the fluid lag-to-cohesive zone size ratio is also small (Bunger et al. 2013; Liu and Lecampion 2021). In this case, a relatively large amount of fluid invades the anticipated large cohesive zone, especially for a low  $\sigma_o/\sigma_c$  ratio (Liu and Lecampion 2021). We again argue that **Eq. (21)** can also be used to estimate  $A_d$ ;
- (v)** The aforementioned conditions **(i)-(iv)** only apply to conventional rocks for which the peak tensile stress (cohesive strength) lies in the range 2MPa to 12MPa (Rybacki et al. 2015). In contrast for brittle materials like PMMA or glass, the tensile strength lies in the range 60 to 70MPa (Zhou et al. 2018), resulting in a very limited extent of the cohesive zone (Garagash 2019). Therefore, for PMMA or glass, **Eq. (19)** is used instead of **Eq. (21)**.

**Table.2** Fracture propagation regimes

Condition	Propagation regime	Fluid Lag	Poiseuille law	Equation for $R_d$ model
$k < 1, \Psi \gg 1$	Viscosity dominated	Significant	Valid	<b>Eq.(19)</b>
$1 \leq k \leq 4, \Psi \ll 1$	Transitional	Minor	Invalid	<b>Eq.(21)</b>
$1 \leq k \leq 4, \Psi \gg 1$	Transitional	Minor	Invalid	<b>Eq.(21)</b>
$\sigma_o/\sigma_c > 1$				
$k > 4$	Toughness dominated	Minor	Invalid	<b>Eq.(21)</b>
PMMA or Glass	Toughness dominated	Significant	Valid	<b>Eq.(19)</b>

### 3. Fracture propagation model validation

#### 3.1 Experimental input data

We use the data of hydraulic fracturing experiments conducted on synthetic rock analogues subjected to true triaxial stress conditions, i.e., e.g., cement/sand blocks from De Pater et al. (1994a), and tight sandstone blocks (Colton and Felser) from Lhomme (2005). These data sets include simultaneous monitoring of wellbore pressure, fracture radius, and strains induced by

hydraulic fracturing. Additionally, corresponding data from two PMMA blocks subjected to biaxial stresses (Bunger et al. 2013) are also considered as a brittle/homogeneous end-member. As shown in **Table 3**, the propagation of hydraulic fractures can be classified as stable or unstable according to the experimental conditions (De Pater et al. 1994a; Lhomme 2005; Bunger et al. 2013). The permeability of Colton 08 and 09 ranges from 0.15 to 0.3mD, while the Cov12c is an order of magnitude lower, i.e., around 0.02mD; fluid leak-off through the fracture walls is therefore ignored. However, the permeability of the Felser sandstone samples are in the range 2 to 5mD, which implies that pressurized fracturing fluid can leak into the pore space of the sample (Lhomme 2005). Based on their petrophysical properties, the seven rock samples are classified into four groups: (i) stable fracture propagation without leak-off, i.e., Cov12c and Colton 08; (ii) stable fracture propagation with leak-off, i.e., Felser 02; (iii) unstable fracture propagation without leak-off, i.e., Colton 09, ab5, c11m1; and (iv) unstable fracture propagation with leak-off, i.e., Felser 03.

In the case of a stable fracture propagation (**Fig.3a**), the early-time fracture nucleation process dissipates a significant amount of energy, resulting in the fracture propagating at a wellbore pressure much lower than the maximum wellbore breakdown pressure, and the rate of wellbore pressure drop to zero is relatively small. The fracture radius and width gradually increase to reach a plateau. In the case of an unstable fracture propagation (**Fig.3b**), fracture initiation and borehole breakdown always coincide. In this situation, the fracture radius and width increase virtually instantaneously, and the wellbore pressure drops approximately ten-times faster than in the stable case.

**Table.3** Materials parameters and experimental conditions from literature (Bunger et al. 2013; De Pater et al. 1994a; Lhomme 2005)

	Sample Type	Young's Modulus E (GPa)	Poisson's Ratio $\nu$ (-)	Permeability K (mD)	Confining Stress $\sigma_o$ (MPa)	Cohesive strength $\sigma_c$ (MPa)	Propagation Condition	Leak-off
Cov12c	Cement/Sand	24	0.25	0.02	9.7	3.5	Stable	No
Colton 08	Very Tight Sandstone	20	0.17	0.15-0.3	10	3	Stable	No
Colton 09	Very Tight Sandstone	14	0.17	0.15-0.3	10	3	Unstable	No
Felser 02	Tight Sandstone	15	0.2	2-5	10	2	Stable	Yes
Felser 03	Tight Sandstone	15	0.2	2-5	10	2	Unstable	Yes
ab5	PMMA	3.3	0.4	0	0	44	Unstable	No
c11m1	PMMA	3.3	0.4	0	0	44	Unstable	No

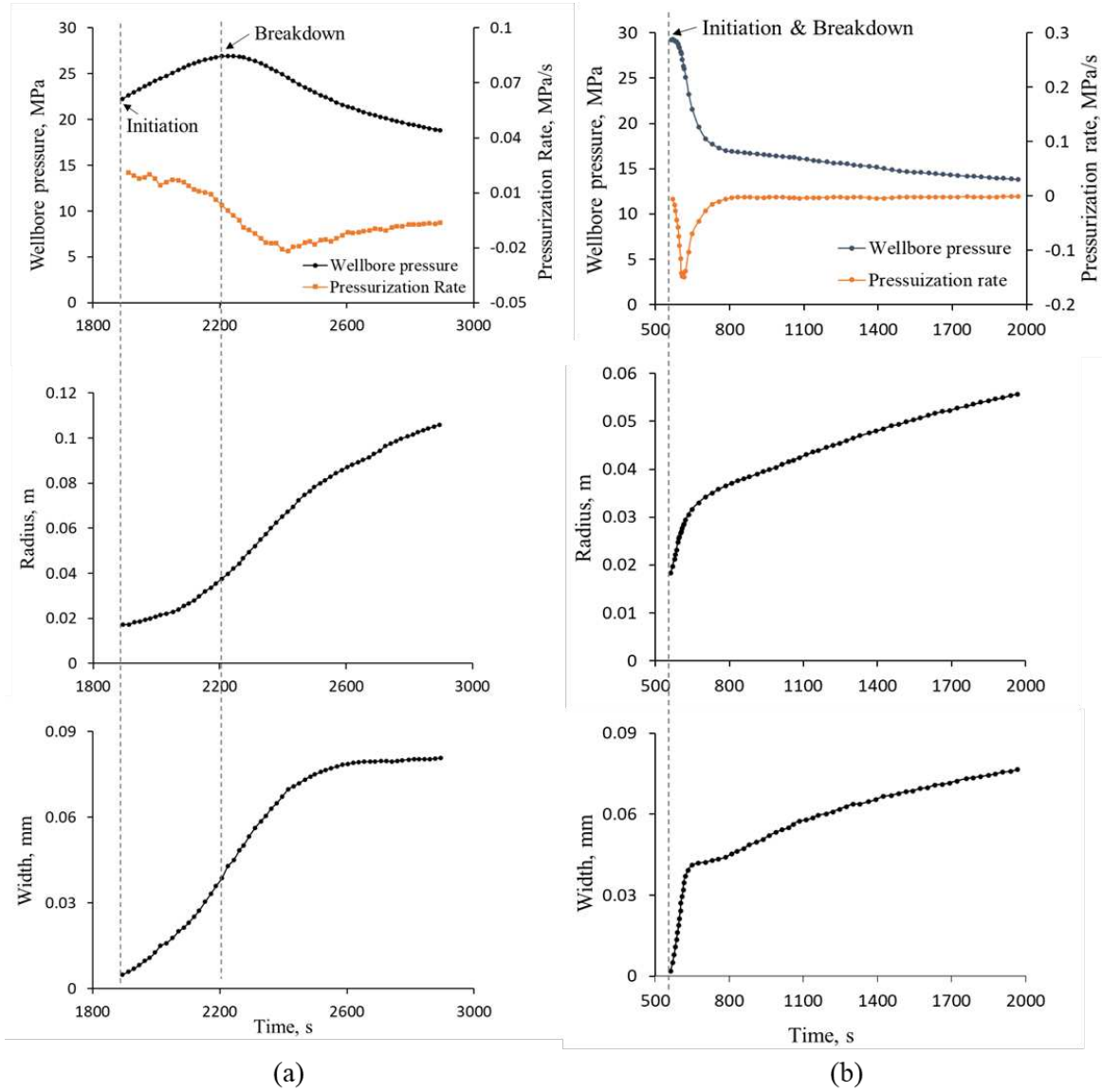


**Fig.3** Experimental results of wellbore pressure, fracture radius, and width (De Pater et al. 1994b; Lhomme 2005): a) Cov12c, stable propagation and b) Felser 03, unstable propagation

### 3.2 Dimensionless parameters

The values of the time scales  $t_{mk}$  and  $t_{om}$ , the dimensionless toughness ( $k$ ), the time scale ratios  $\chi$  and  $\Psi$ , and the ratio of confining stress to cohesive strength ( $\sigma_o/\sigma_c$ ) for each sample are reported in **Table 4**. These dimensionless parameters are used here to predict the characteristics of fracture propagation in terms of stability.

#### 3.2.1 Stable fracture propagation

- **Sample Cov12c:** The dimensionless toughness  $k = 0.43$  indicates that the propagation regime is strongly viscosity-dominated; and  $\Psi \gg 1$  indicates that there is strong fluid lag during propagation. Therefore, **Eq. (19)** based on Poiseuille's flow law is used for the prediction of the fracture's radius  $R_d$ .

- **Sample Colton 08:** The  $k = 1.20$  indicates a transition from a viscosity- to a toughness-dominated propagation regime; and  $\Psi \ll 1$  indicates that fluid lag is negligible during the propagation. Therefore, **Eq. (21)** based on the modified Poiseuille's flow law is used to estimate  $R_d$ .
- **Sample Felsler 02:** The  $k = 1.86$  also indicates a transition from a viscosity- to a toughness-dominated propagation regime; and  $\Psi = 215$  indicates that fluid lag can occur; however, the relatively large ratio  $\sigma_o/\sigma_c = 5$  for  $k = 1.86$  suggests that the fraction of fluid lag to cohesive zone is relatively small (Liu and Lecampion 2021). Therefore, **Eq. (21)** is again used to estimate  $R_d$ .

### 3.2.2 Unstable fracture propagation

- **Sample Felsler 03:** The  $k = 3.4$  indicates that the fracture propagation regime is essentially toughness dominated; and  $\Psi = 21.5$  implies that fluid lag can occur, although this effect is partly compensated by the relatively large stress ratio  $\sigma_o/\sigma_c = 5$ , which tends to accelerate fluid flow into the process zone, and reduce the fluid lag-to-cohesive zone ratio. Therefore, **Eq. (21)** used to estimate  $R_d$ .
- **Sample Colton 09:** The  $k = 3.0$  indicates that the fracture propagation regime is essentially toughness dominated; and  $\Psi = 3.5$  and  $\sigma_o/\sigma_c = 3.33$  suggest that fluid lag is relatively negligible during propagation. Therefore, **Eq. (21)** is used to estimate  $R_d$ .
- **Samples ab5 and c11m1 (PMMA):** The  $k = 3.5$  for sample ab5, and  $k = 5.3$  for sample c11m1 indicate that the fracture propagation regime is essentially toughness dominated. These experiments were conducted in the laboratory under the condition  $\sigma_o/\sigma_c = 0$  to allow for high-resolution monitoring of the propagation with a high-speed camera through the transparent PMMA samples. In this situation, fluid lag was not observed during propagation (Bunger 2005; Bunger et al. 2013). Numerical simulations also suggest a very limited fluid lag (Liu and Lecampion 2021). The most important is that the tensile strength (peak cohesive strength) of PMMA is larger than 60MPa (Zhou et al. 2018), which is orders of magnitude larger than for rocks, resulting in a very limited extent of the cohesive zone (Bunger and Detournay 2008; Garagash 2019). Therefore, fluid flow is expected to follow Poiseuille's law, and **Eq. (19)** is used to estimate  $R_d$  for PMMA.

**Table.4** Experimental propagation duration(s), viscosity-toughness transition time scale  $t_{mk}$ , fluid lag time scale  $t_{om}$ , dimensionless toughness  $k$ , time scale ratios  $\chi$ ,  $\Psi$  by constant injection rate  $Q_0$ , and ratio of confining stress to cohesive strength ( $\sigma_o/\sigma_c$ )

	Propagation Duration(s)	$t_{mk}$ (s)	$t_{om}$ (s)	$k$	$\chi = \frac{t_{mk}}{t_m^k}$	$\Psi = \frac{t_{mk}}{t_{om}}$	$\sigma_o/\sigma_c$
COV12c	1002	2.23e+06	1181	0.43	235	1886	2.77
Colton 08	2268	421	2545	1.2	0.37	0.17	3.33
Colton 09	10.6	18	5	3.0	0.45	3.51	3.33
Felser 02	2466	3.15e+05	1465	1.86	38	215	5
Felser 03	1404	787	37	3.4	3.3	21.5	5
ab5	4.3	2.1	N/A	3.5	0.59	N/A	0
c11m1	9.2	0.1	N/A	5.3	0.06	N/A	0

### 3.3 Dynamic fracturing area ( $A_d$ ) validation

Here we validate the model of fracture area  $A_d$  for a stable propagation using published data detailed in Section 3.1 and 3.2. Four typical cases are presented in this section:

- (i) Stable propagation for a strong viscosity dominated regime ( $k=0.43$ ) in a tight cement-sand sample, i.e., Cov12c
- (ii) Stable propagation for a transitional propagation regime ( $k=1.2$ ) in a very tight sandstone, i.e., Colton08
- (iii) Unstable propagation for a toughness dominated regime ( $k=3.0$ ) in a very tight sandstone, i.e., Colton09
- (iv) Unstable propagation for a strong toughness dominated regime ( $k=5.3$ ) in a very hard material-PMMA, i.e., C11m1

For the validation of Felser 02 and 03 where the leak-off may affect the hydraulic fracture propagation, are presented in Appendix.B.1 and B.3. For ab5, it is repeated to PMMA c11m1, and the validation is listed in the Appendix B.2.

#### 3.3.1 Stable fracture propagation (no leak-off)

##### **Cov12c:**

The evolution of the fracture area with time  $A_d(t)$  in the cement-sand sample measured by De Pater et al (1994) and predicted with the new  $A_d$  model are displayed in **Fig.4**. **Fig.4a** shows that the incremental fracture area per time step  $(\Delta A_r)_m$  correlates well with the product  $PD_1 = \sqrt{-\frac{w_m^2}{12\mu_f} \left(\frac{\Delta p_f}{\Delta t}\right)_m}$ . The resulting linear correlation shown in **Fig.4b** validates a posteriori the linearity assumption stated in section 2.2, i.e.,

$$(\Delta A_r)_m = 3.06 \times 10^3 \times \sqrt{-\frac{w_m^2}{12\mu_f} \left(\frac{\Delta p_f}{\Delta t}\right)_m} - 5.55 \times 10^{-7}, \text{ with } R^2 = 0.96 \quad (29)$$

where the value of the y-axis intercept  $B = -5.55 \times 10^{-7} \ll (\Delta A_r)_m$ . Therefore, **Eq.(17)** can behave similar to **Eq.(18)**. Considering this correlation, the time evolution of the dimensionless parameter of relative change in fracture area  $(\Delta A_r)_m/A_T$  and the fraction

$$\frac{\sqrt{-\frac{w_m^2}{12\mu_f} \left(\frac{\Delta p_f}{\Delta t}\right)_m}}{\sum_{i=1}^N \sqrt{-\frac{w_i^2}{12\mu_f} \left(\frac{\Delta p_f}{\Delta t}\right)_i}} \quad \text{are calculated and shown in Fig.4c, indicating a}$$

reasonably robust fit, despite some measurement-induced fluctuations in  $(\Delta A_r)_m/A_T$ . Finally,

**Fig.4d** compares the predicted evolution of the fracturing area  $A_d$  (red triangle) and the experimental data (black dots).

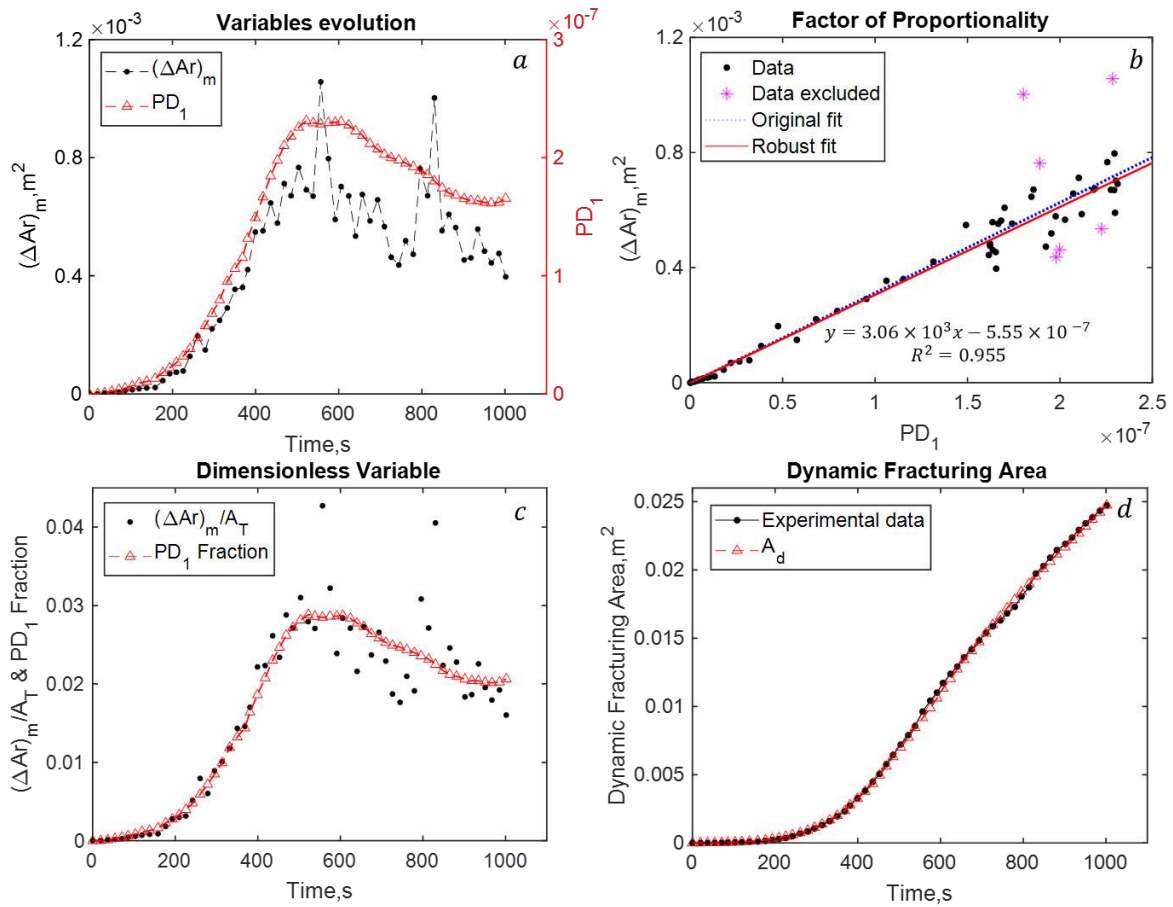


**Fig.4** Evolution of the fracture area for the cement/sand sample during stable propagation; Comparison between direct laboratory measurements and predictions of the new model presented here.

### **Colton 08:**

The evolution of the fracture area with time in Colton 08 experimentally measured by Lhomme (2005) and analytically predicted by our  $A_d$  model is presented in **Fig.5**. Based on the aforementioned dimensionless parameters, and the experimental evidence of cohesive zone in Colton sandstone (Garagash 2019; Lhomme 2005), the cohesive zone effects are accounted for

(see **Eqs.20 and 21**) for Colton 08. Similar to Cov12c, we obtain reasonably good linear correlation (**Fig.5b**):

$$(\Delta A_r)_m = 15.59 \sqrt[3]{-\frac{w_m^2}{12\mu_f} \left(\frac{\Delta p_f}{\Delta t}\right)_m} - 8.24 \times 10^{-6}, \text{ with } R^2 = 0.9 \quad (30)$$

A good fit is observed between our analytical prediction and the experimental measurement shown in **Figs.5c** and **5d**, validating the postulation and approach followed here.

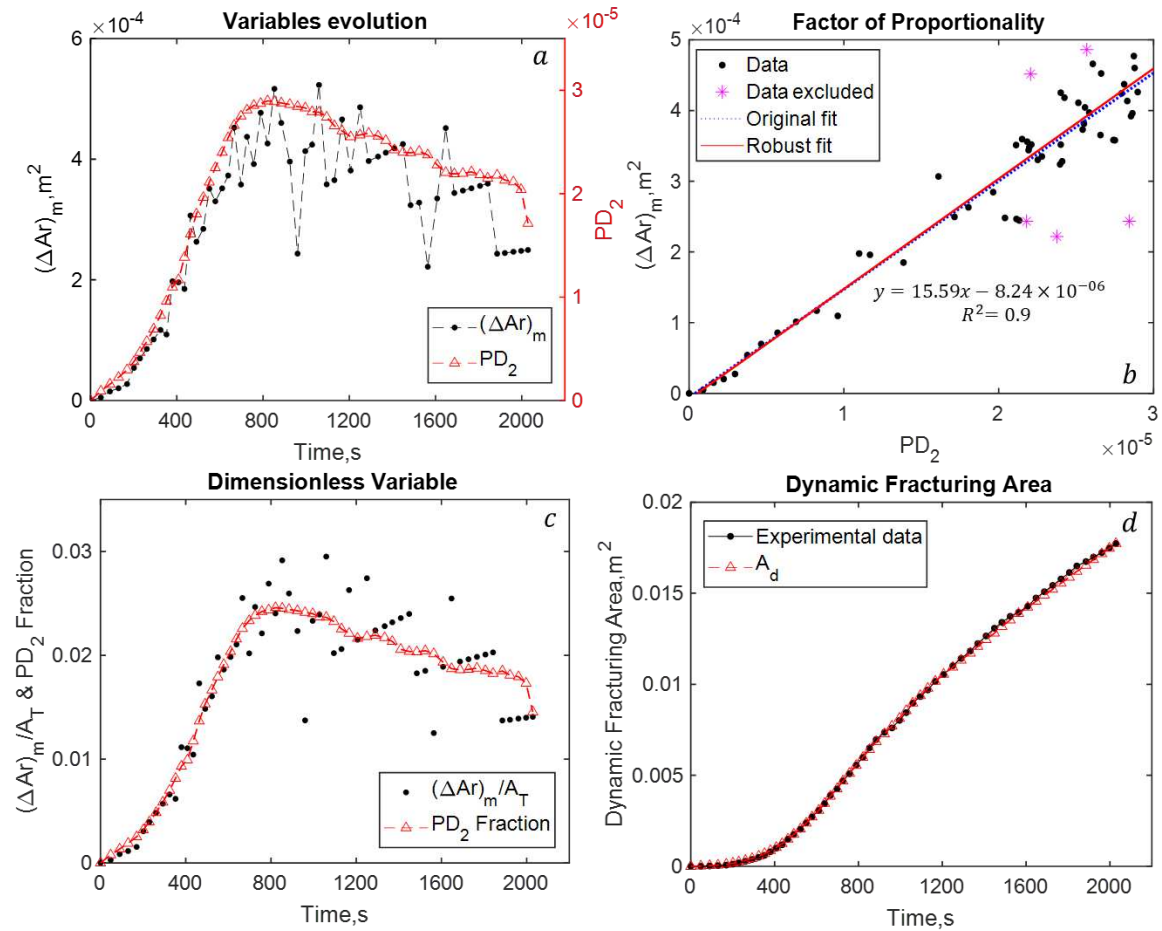


**Fig.5** Evolution of the fracture area for the Colton 08 sandstone sample during stable propagation; Comparison between direct laboratory measurements and predictions of the new model presented here.

### 3.3.2 Unstable fracture propagation (no leak-off)

Here we validate the model of fracture area  $A_d$  for an unstable propagation using published data detailed in Section 3.1, i.e., **Colton 09 and c11m1** samples for which no leak-off is expected.

#### **Colton 09 and c11m1:**

The evolution of the fracture area with time measured by Lhomme (2005) in the Colton 09 sample, and by Bungler et al. (2013) in the PMMA c11m1 sample, along with the prediction from the new  $A_d$  model are shown in **Figs. 6 and 7**, respectively. Analogously to the case of stable propagation, we obtain reasonably good linear correlations, i.e.,

$$(\Delta A_r)_k = 0.14 * \sqrt[3]{-\frac{w_k^2}{12\mu_f} \left(\frac{\Delta p_f}{\Delta t}\right)_k} - 2.28e - 07, \text{ with } R^2 = 0.95 \quad (31)$$

for the Colton 09 sample, and

$$(\Delta A_r)_k = 1.35 * \sqrt[3]{-\frac{w_k^2}{12\mu_f} \left(\frac{\Delta p_f}{\Delta t}\right)_k} - 1.37e - 08, \text{ with } R^2 = 0.92 \quad (32)$$

for the PMMA c11m1 sample. Such good fits validate the approach a posteriori.

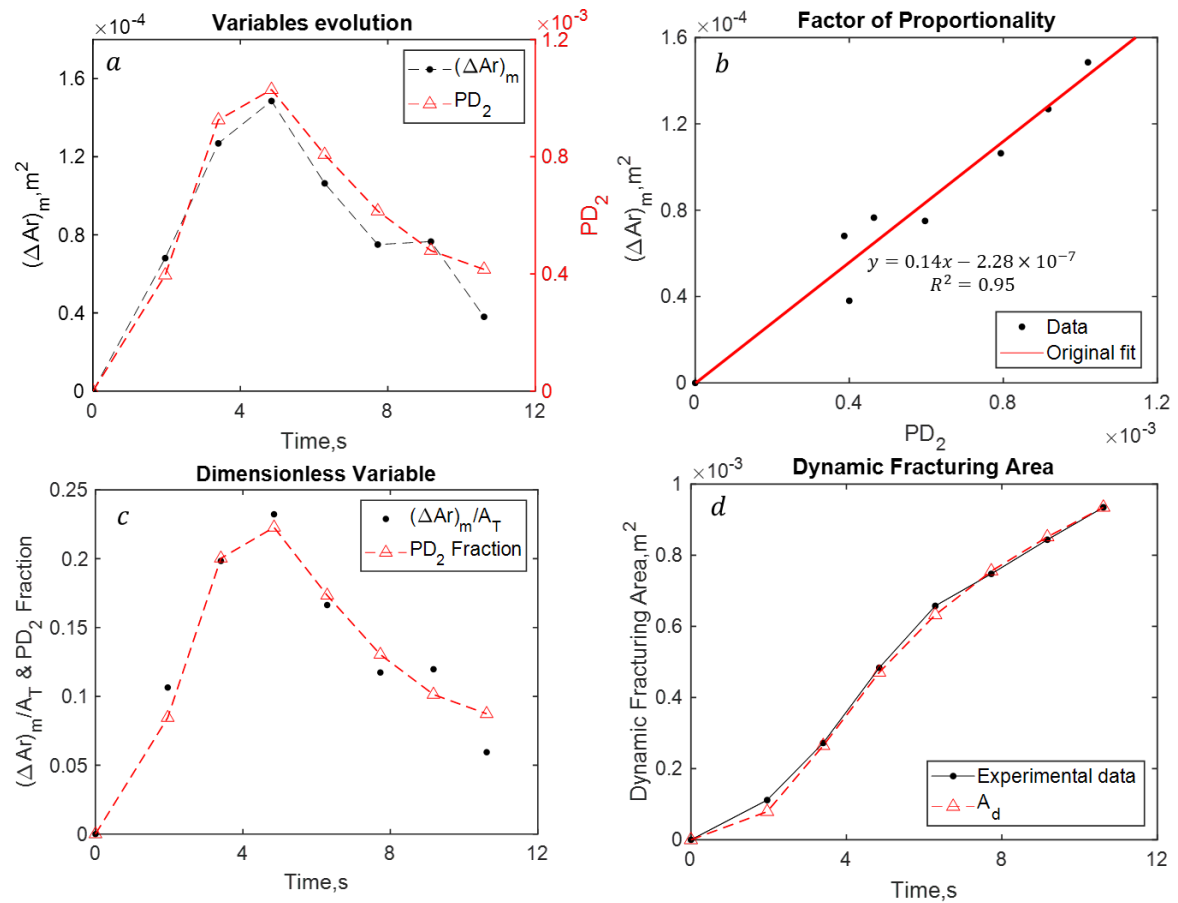


**Fig.6** Evolution of the fracture area for the Colton 09 sandstone sample during unstable propagation; Comparison between direct laboratory measurements and predictions of the new model presented here.

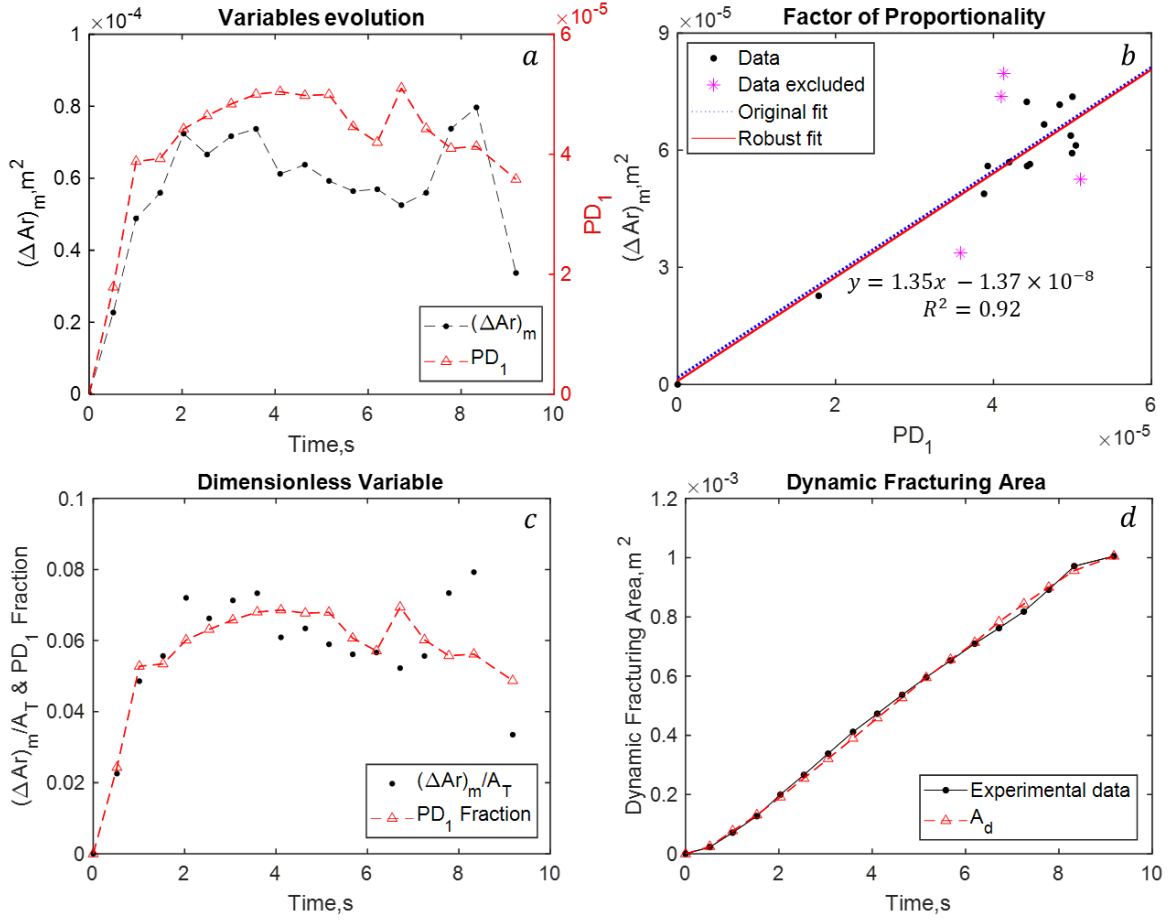


**Fig.7** Evolution of the fracture area for the PMMA sample c1 1m1 during unstable propagation; Comparison between direct laboratory measurements and predictions of the new model presented here.

#### 4. Results (Comparison of the elastic and hydraulic fracturing models)

For the seven samples detailed in **Table 3**, we compare here the radius predictions of the elastic fracture model ( $R_E$ ), and the new model based on Poiseuille's flow law ( $R_d$ ). For  $R_E$ , the fracture width measured in the laboratory is anticipated to be maximum at the wellbore; therefore, **Eq.(9)** is used. On the other hand, the new  $R_d$  model is detailed in Section 2.22, and applied to the seven samples as detailed in Section 3.2, i.e., the use of **Eqs. 19 or 21**.

##### 4.1 Stable fracture propagation

###### 4.1.1 Without leak-off

For this situation we consider the cement/sand sample Cov12c and one ultra-tight sandstone sample Colton 08. The time evolution of the fracture radius as predicted by the two models  $R_E$  and  $R_d$  are compared to the experimentally-estimated radius in **Fig.8**.

For both samples **Cov12c (Fig.8a)** and **Colton 08 (Fig.8b)**, the predicted radius  $R_d$  agrees well with experimental data, for the entire propagation period. For sample **Cov12c (Fig.8a)**, the predicted radius  $R_E$  slightly over-estimates the measured radius at early time ( $T < 600s$ ), but severely under-estimates it at larger time ( $T > 600s$ ). Interestingly, for **Colton 08 (Fig.8b)**, the predicted radius  $R_E$  is in relatively good agreement with experimental data, except for the very late propagation stage  $t > 1600s$ .

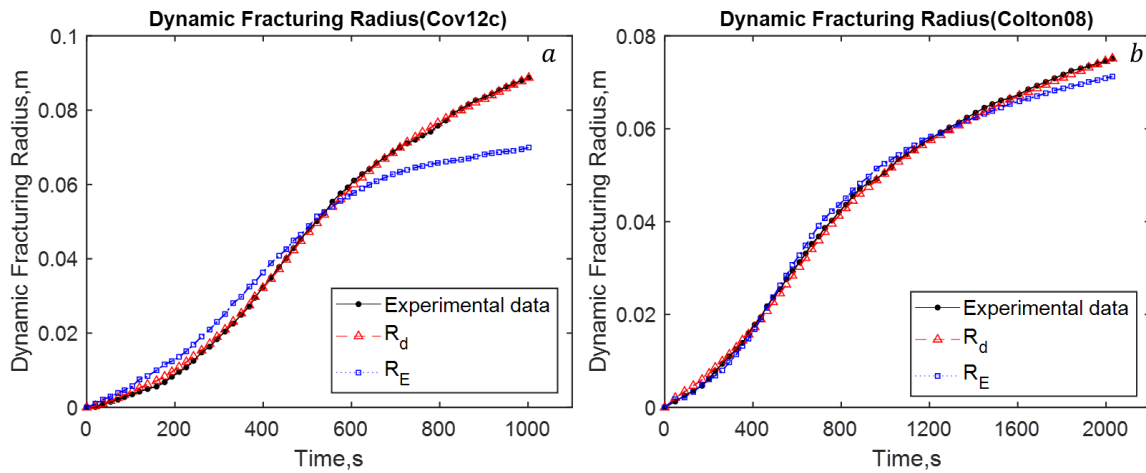


**Fig.8** Dynamic fracturing area based on elasticity theory,  $R_d$  model, and experimental data: a) Cov12c; b) Colton 08

#### 4.12 With leak-off

For this situation we consider the sandstone sample **Felser 02 (Fig.9)**. The predicted radius  $R_d$  matches well the experimental data, whereas the predicted  $R_E$  significantly under-estimates the measured radius for the entire propagation period. Fluid loss (leak-off) through the fracture's wall during fracturing is a plausible cause for the smaller fracture radius reached at a given time during fracture propagation (Lhomme 2005).

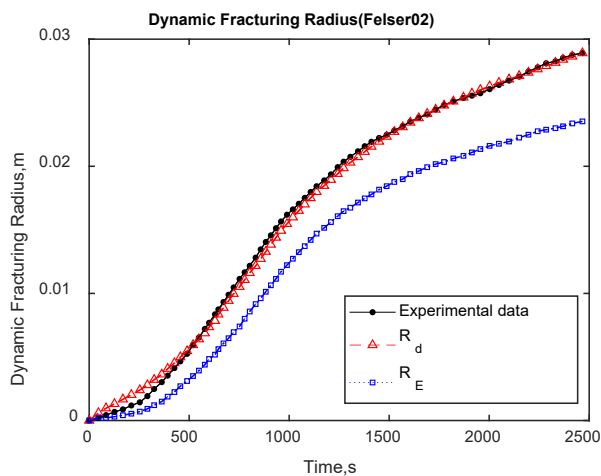


**Fig.9** Dynamic fracturing area based on elasticity theory,  $R_d$  model, and experimental data-Felser 02

Overall, for a stable fracture propagation (**Figs.8 and 9**), we observe a good agreement between the  $R_d$  model predictions and the experimental data. On the other hand, the  $R_E$  model predictions exhibit more deviation from the experimental data in the transitional propagation regime ( $k = 1.2$ ) with negligible fluid lag ( $\Psi \ll 1$ ), i.e., for the **Colton 08** sample. Even more significant deviations are observed when the propagation regimes are dominated by viscous dissipation (e.g.,  $k = 0.43$  for the **Cov12c** sample; or when leak-off occurs for the **Felser 02** sample).

## 4.2 Unstable fracture propagation

### 4.2.2 Without leak-off

For situation we consider the ultra-tight sandstone sample **Colton 09**, the two PMMA samples **ab5** and **c11m1**, and the tight sandstone sample **Felser 03**. The time evolution of the fracture radius as predicted by the two models  $R_E$  and  $R_d$  are compared to the experimentally-estimated radius in **Figs. 10 and 11**. For the **Colton 09** sample (**Fig.10a**), the propagation time is less than 12 seconds to reach a final radius of approximately 0.02m. The  $R_d$  model predictions agree well with experimental data. However, the  $R_E$  radius prediction is significantly biased, which is attributed to the anomalous fracture width recorded during this unstable fracture propagation (Lhomme 2005). Again for the two PMMA samples **c11m1** (**Fig. 10b**) and **ab5** (**Fig. 10c**), the predicted  $R_d$  compares well with experimental data, whereas the predicted  $R_E$  significantly deviates, i.e., over-estimation for the c11m1 sample, and under-estimation for the ab5 sample.

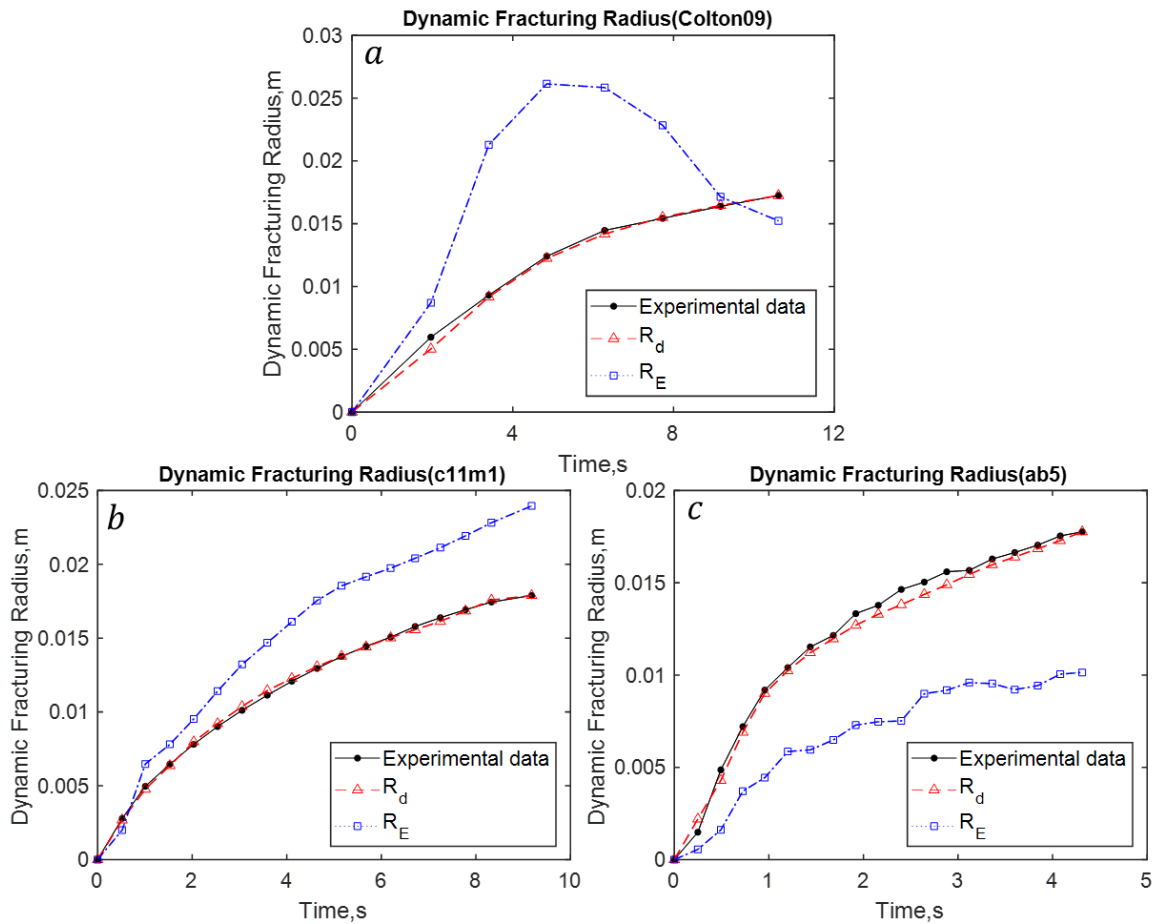


**Fig.10** Dynamic fracturing area based on elastic theory,  $R_d$  model, and experimental data- a) Colton 09; b) c11m1; c) ab5

#### 4.23 Unstable Cases (leak-off)

For this situation we consider the **Felser 03** sample (**Fig.11**). The  $R_d$  predictions agree well with experimental data, except for the intermediate period from 40 to 190s. This is attributed to the transition from strongly unstable to steady fracture propagation. On the other hand, the  $R_E$  predictions exhibit a significant and growing deviation from experimental data with time, except at early times up to 50s.

Overall, for unstable fracture propagation, the  $R_d$  model predictions compare well with experimental data, whereas the  $R_E$  model performs poorly for similar fracture propagation conditions.

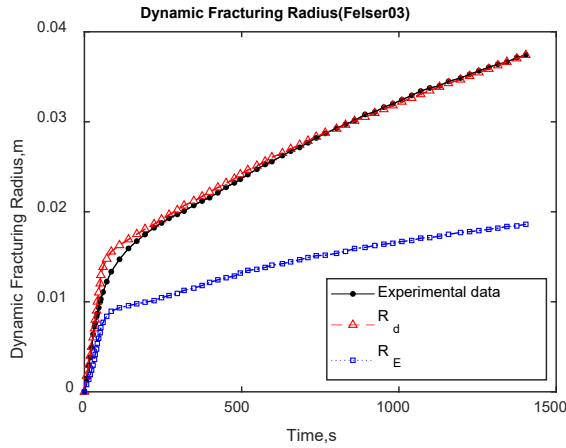


**Fig.11** Dynamic fracturing area based on elasticity theory,  $R_d$  model, and experimental data-Felser 03

## 5. Discussion and Implications

### 5.1 Validation of the Poiseuille flow within hydraulic fracture

We confirm that the near-tip cohesive zone plays a critical role during the propagation of a hydraulic fracture in conventional rocks having a tensile strength ranging from 2 to 12 MPa when in situ stress conditions at depth induce a high  $\sigma_o/\sigma_c$  ratio. In the viscosity-dominated propagation regime with significant fluid lag (Cov12c), and where the cohesive zone is embedded in the lag zone (see **Fig.1b**), the conventional Poiseuille flow law is acceptable. In contrast, when a relatively small fraction of fluid lag is embedded in the cohesive zone (**Fig.1c** for Colton 08 and 09), the linear relationship between width  $w$  and velocity  $u$  must be modified to a fractional power dependence  $w \propto \left(\frac{dr}{dt}\right)^{\frac{3}{2}}$  (see **Eqs.20 and 21**) for  $R_d$ . For materials like PMMA with a relatively higher tensile strength (above 60MPa), the impact of the cohesive zone on fracture propagation is very limited, which in turn suggests that the conventional Poiseuille flow law and Linear elastic fracture mechanics (LFEM) can be used under such conditions.

### 5.2 Validity of the linear relationship between the incremental fracturing area ( $\Delta A_r$ )m and the product PD

The linearity between  $(\Delta A_r)_m$  and  $PD$  is an important indicator of a successful  $R_d$  modelling. For both stable and unstable fracture propagation without leak-off, this linearity is evident, resulting in a good agreement of the model with experimental data for most samples for which direct measurement of the fracture radius evolution with time is available in the literature (see Tables 3 and 4, and **Figs. 4b, 5b, 6b, 7b, and A2b**). On the other hand, when leak-off effects

play a role in relatively permeable samples, e.g., Felser 02 in **Fig.A1b** and Felser 03 in **Fig.A3b**, the linear regression between  $(\Delta A_r)_m$  and  $PD$  is less robust, resulting in some discrepancy between  $R_d$  predictions and experimental data.

Porosity may also affect the aforementioned relationship; the more porous the rock, the more irreversible deformation is recorded during hydraulic fracturing according to (Holt et al. 2015; Wong and Baud 2012) for instance. This is qualitatively consistent with the porosity measured in the Felser 02 and 03 sandstone samples ( $\Phi = 0.21$ ), the Colton sandstone ( $\Phi = 0.12$ ), and the cement/sand composite Cov12c ( $\Phi = 0.15$ ).

### 5.3 Applicability of the $R_E$ and $R_d$ models

The results indicate that the first model based on linear elasticity ( $R_E$ ) can only be applied in very limited circumstances, such as outside the viscosity-dominated regime ( $k > 1$ ) with negligible fluid lag ( $\Psi \ll 1$ ) under stable propagation (**Fig.8b**). However, for fracture propagation under various conditions, the  $R_E$  model performs poorly (**Figs.8a, 9, 10, and 11**). The results also show that the new  $R_d$  model matches well the experimental data, regardless of the propagation regimes, the stability of the propagation, or whether leak-off occurs. Such a broad applicability is due to the fact that this model is based on a mechanistic approach and involves self-similarity, dimensional analysis and direct laboratory observations (**Eqs. 15, 16, 17**). This suggests that the  $R_d$  model can be robustly applied in the laboratory, and is likely to perform well in the field as well.

## 7. Conclusion and Recommendations

Hydraulic fracture propagation is a complex and coupled process involving fluid-solid interactions, integrating multiscale propagation regimes with stability conditions to be accounted for under varying stress regimes (e.g., depth, proximity to major tectonic faults, etc.). This significantly challenges our ability to predict/control the propagation of hydraulic fractures, and the fate of fracturing fluids underground.

We thus present two models for dynamic radius prediction of penny shaped fracture at depth: where the first model relies on the modified linear elasticity ( $R_E$ ); the second follows the Poiseuille's law under the assumption of self-similarly fracture propagation ( $R_d$ ), which is validated through published experimental data, i.e., hydraulic fracturing of five synthetic/natural tight sandstones under true tri-axial stress, and two PMMA under biaxial stress conditions.

The modelling exercise shows that the cohesive zone plays an important role in hydraulic fracturing for conventional rocks ( $2 \leq \sigma_c \leq 12\text{MPa}$ ): i) The Poiseuille flow within hydraulic fracture is only valid for the propagation condition under high viscosity dominated ( $k \ll 1$ ) propagation with significant fluid lag ( $\Psi \gg 1$ ) and ii) For the condition in which the small fraction of fluid lag is embedded in the cohesive zone (**Fig.1c**), the proportionality  $w \propto \frac{dr}{dt}$  is required to be modified as  $w \propto \left(\frac{dr}{dt}\right)^{\frac{3}{2}}$  used in  $R_d$  model.

The first model based on linear elasticity ( $R_E$ ) can only be applied for very limited conditions, i.e., non-viscous dominated regimes with negligible fluid lag under stable propagation. On the other hand, the good agreement between the results from our  $R_d$  model and experimental data indicates that experimental radius of hydraulic fracture under true tri-axial stress condition can be properly reconstructed by  $R_d$ :

- (i) The self-similarity of radially hydraulic fracture propagation is valid for laboratory scaled experiments.
- (ii) For the conditions, i.e., the boundary, fracture displacement, and wellbore pressure are obtained from laboratory or field investigations, our  $R_d$  model takes advantages of the dynamic radius prediction of finite hydraulic fracture under the rigorous conditions (e.g., multiscale propagation regimes, stable/unstable propagation, leak-off effect), and moreover, it facilitates a simple mathematical formulation and low computational cost.
- (iii) Field assessment of  $R_d$  model is recommended, where the radius predicted from  $R_d$  can be applied for the calibration of fracture growth monitoring based on active/passive seismic interpretation.

### **Declaration of competing interest**

The authors declare that they have no known competing interest

### **Acknowledgments**

The first author sincerely thanks China Scholarship Council- Curtin International Postgraduate Research Scholarship (CSC-CIPRS, Grant No. 201808190001) for their financial support on this research.

## Appendix. A: $\frac{\partial p_f}{\partial t}$ Correction for early-time initiation

When the process of early-time fracture initiation is significant, i.e., the fracture initiates at a much lower wellbore pressure than the breakdown pressure (i.e. maximum pressure recorded during the entire test), which is mostly happened in stable propagation cases, e.g., hydraulic fracturing tests reported in Lhomme (2005), Sarmadivaleh (2012), and Lecampion et al. (2017).

Therefore, the pressurization rate ( $\frac{\partial p_f}{\partial t}$ ) stay positive until reaches to the breakdown pressure,

for convenience of calculating the *product*  $\sqrt{-\frac{w^2}{12\mu_f} \frac{\Delta p_f}{\Delta t}}$ , the pressurization rate for early-time fracture propagation ( $\frac{\partial p_f}{\partial t}_{ei}$ ) can be corrected as:

$$\frac{\partial p_f}{\partial t}_{ei} = \frac{\partial p_f}{\partial t} - \frac{\partial p_f}{\partial t}_{pri} \quad (A1)$$

where  $\frac{\partial p_f}{\partial t}_{pri}$  is the linearized wellbore pressurization rate before fracture initiation.

For stable propagation case (i.e., significant early-time initiation & propagation), the correction of  $\frac{\partial p_f}{\partial t}$  (Eq.13) will be only applied prior to maximum wellbore pressure. On the other hand, for unstable propagation case where the initiation and breakdown of wellbore pressure always coincide, the effective pressurization rate ( $\frac{\partial p_f}{\partial t}_{ei}$ ) will be used for the entire propagation due to the wellbore storage effect (Lecampion et al. 2017).

## Appendix. B Dynamic fracturing area ( $A_d$ ) validation for leak-off and repeated case

### B.1. Felsler 02: Stable propagation case with leak-off

The evolution of the fracture area with time measured by Lhomme (2005) in Felsler 02 is displayed in **Fig.6**. Similar to Colton 08, the cohesive zone effect are also necessarily accounted. As shown in **Fig.6a**, the  $(\Delta A_r)_m$  exhibited reasonably analogous trend with the

*product*<sub>2</sub>  $\sqrt[3]{-\frac{w_m^2}{12\mu_f} \left(\frac{\Delta p_f}{\Delta t}\right)_m}$ , albeit stronger fluctuation of  $(\Delta A_r)_m$  is observed after the peak. The

robust linear regression analysis of  $(\Delta A_r)_m$  verse  $PD_2$  indicates a weakly linear relation with  $R^2 = 0.84$  (**Fig.6b**):

$$(\Delta A_r)_m = 3.07 * \sqrt[3]{-\frac{w_m^2}{12\mu_f} \left(\frac{\Delta p_f}{\Delta t}\right)_m} + 1.79 \times 10^{-6} \quad (A2)$$

The time evolution of the dimensionless relative change in experimental fracture area

$$(\Delta A_r)_m / A_T \text{ and the analytical fraction } \frac{\sqrt[3]{-\frac{w_m^2}{12\mu_f} \left(\frac{\Delta p_f}{\Delta t}\right)_m}}{\sum_{i=1}^N \sqrt[3]{-\frac{w_i^2}{12\mu_f} \left(\frac{\Delta p_f}{\Delta t}\right)_i}} \text{ are shown in}$$

**Fig.6c**, indicating a reasonably robust fit, despite some fluctuations in measured  $(\Delta A_r)_m / A_T$ .

Finally, **Fig.6d** compares the predicted evolution of the fracturing area  $A_d$  (red triangle) and the experimental data (black dots), validating the hypothesis and approach followed here.

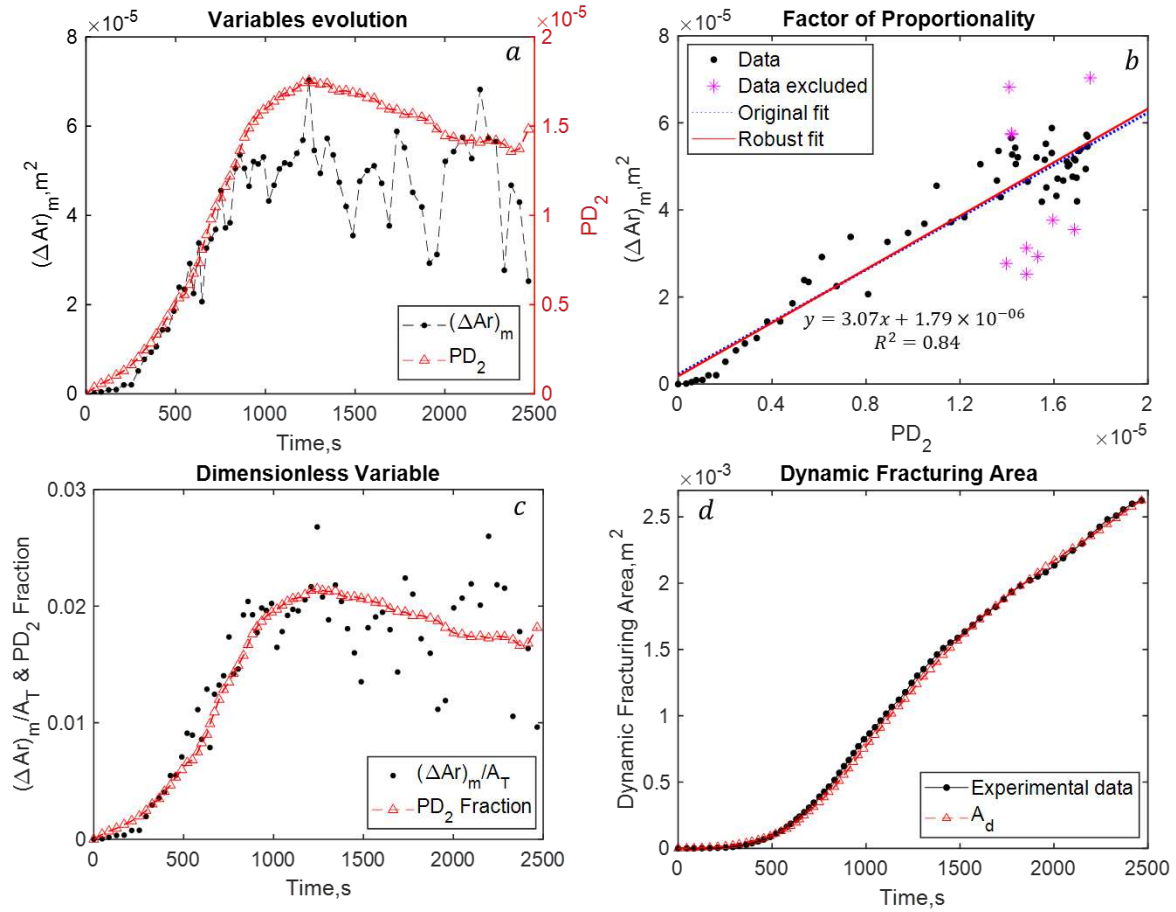


**Fig.A1** Evolution of the fracture area for the Felser 02 sandstone sample during stable propagation: Comparison between direct laboratory measurements and predictions of the new model presented here.

## B.2. ab5: Unstable propagation case(no leak-off)

The evolution of the fracture area with time measured by Bungert et al. (2013) in ab5 and the prediction from our  $A_d$  model are shown in **Fig.8**. Analogously to the previous PMMA case(c11m1), we obtain the reasonably good linear correlation **Fig.8b**:

$$(\Delta A_r)_m = 2.9 * \sqrt{-\frac{w_m^2}{12\mu_f} \left(\frac{\Delta p_f}{\Delta t}\right)_m} - 3.07e - 06, \quad R^2 = 0.93 \quad (\text{A3})$$

Accounting for these correlations, **Fig.8d** show the final results for the two corresponding samples. Again, a reasonable fit is found between predicted and measured evolution of the fracture area, although the minor discrepancy is observed during the intermediate propagation time.

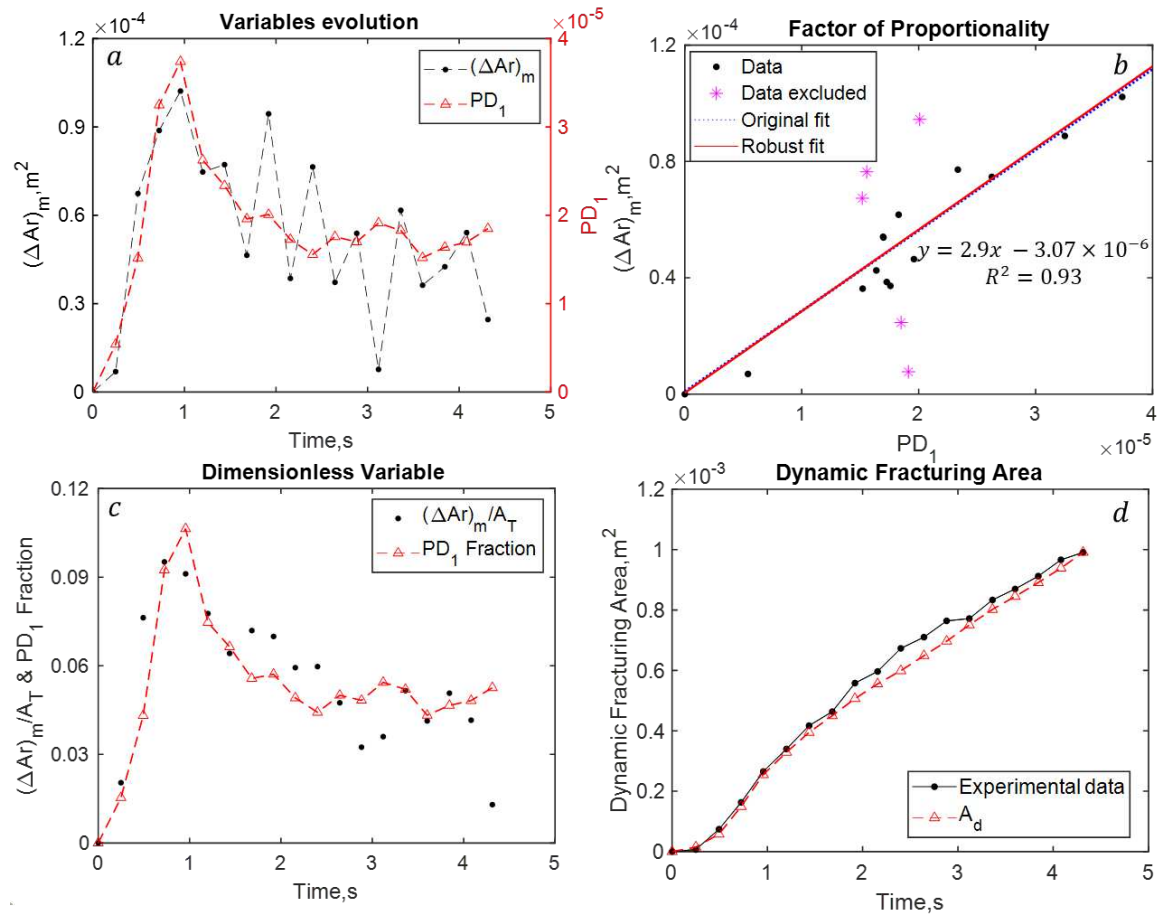


**Fig.A2** Evolution of the fracture area for the ab5 (PMMA sample) during stable propagation: Comparison between direct laboratory measurements and predictions of the new model presented here.

### B.3. Felser 03: Unstable propagation case with leak-off

Unlike the unstable cases with non-leak-off (i.e., Colton 09, ab5, and c11m1), for Felser 03 the value of  $(\Delta A_r)_m$  significantly scatter after propagation of 50s (**Figs.10a and c**), resulting in a weak linearity between  $(\Delta A_r)_m$  and  $PD_2$  (**Fig.10b**) :

$$(\Delta A_r)_m = 7053 * \sqrt[3]{-\frac{w_m^2}{12\mu_f} \left(\frac{\Delta p_f}{\Delta t}\right)_m} - 9.1e - 07, R^2 = 0.76 \quad (34)$$

The linear regression analysis indicates that the proportional hypothesis between  $(\Delta A_r)_m$  and  $PD_2$  is partially valid; the value of y-axis intercept  $B$  are still negligible since  $B \ll (\Delta A_r)_m$ .

Although the dimensionless variable  $(\Delta A_r)_m / A_T$  are highly fluctuated after 50s (Fig.10c), the dynamic fracturing area(Eq.11) are in relatively good agreement with the experimental data.

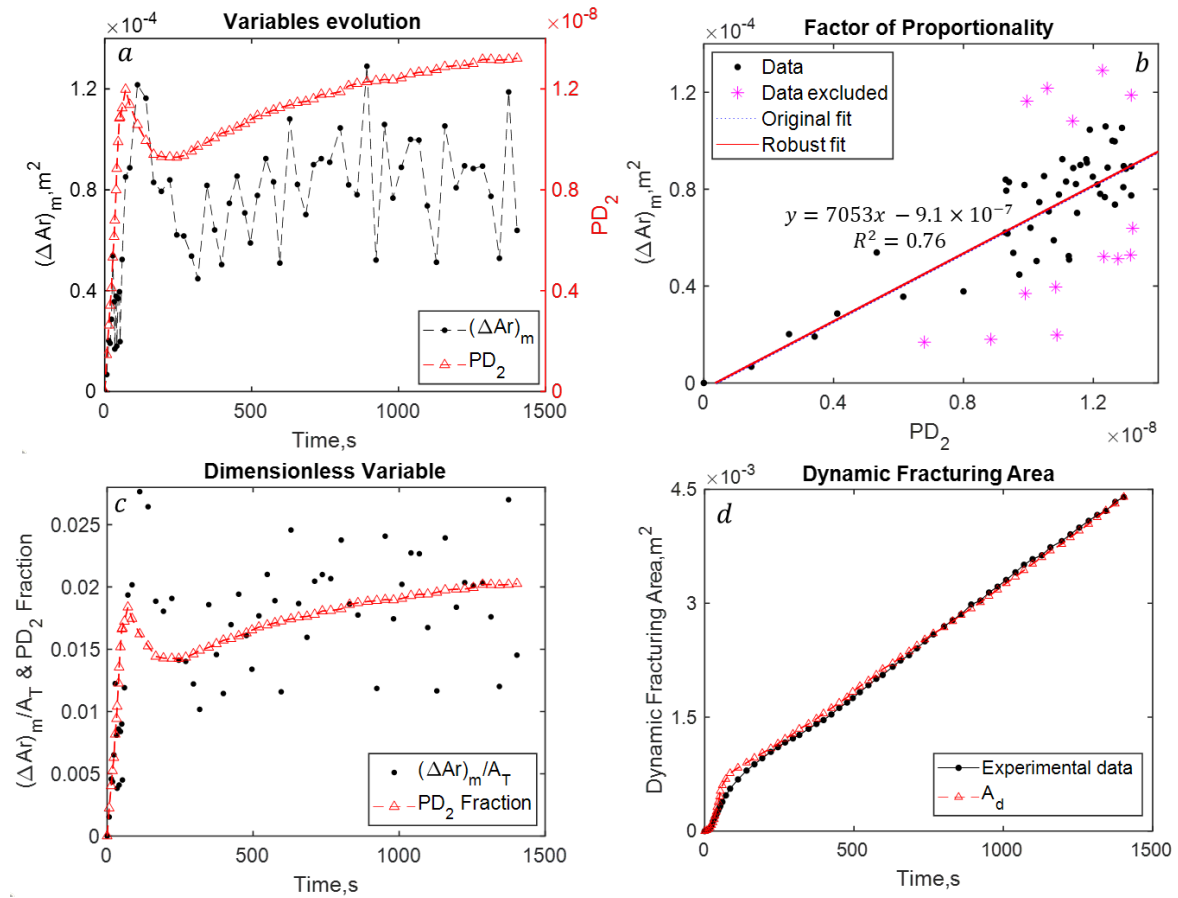


**Fig.A3** Evolution of the fracture area for the Felser 03 during stable propagation: Comparison between direct laboratory measurements and predictions of the new model presented here.

### Abbreviations

<i>TTSC</i>	True tri-axial stress condition
<i>TTSCs</i>	True tri-axial stress cell
<i>UCS</i>	Uniaxial compressive strength
<i>TCS</i>	Tri-axial compressive strength
<i>BHP</i>	Wellbore pressure
<i>PMMA</i>	Polymethyl Methacrylate
<i>LEFM</i>	Linear Elastic Fracture Mechanics
<i>md</i>	MiliDracy

### List of Symbols

$Q_o$	Constant injection rate supplied by pump
$q$	Flow rate per unit perimeter
$P_f$	Fluid pressure
$u$	Fluid velocity
<i>BHP</i>	Wellbore pressure
$w$	Width of hydraulic fracture
$A_r$	Fracture surface area

$\Delta t_{\kappa}$	Arbitrary unit time increment
$(\Delta A_r)_{\kappa}$	Incremental increase in fracture surface area per unit time increment $\Delta t_{\kappa}$
$\lambda$	Factor of proportionality
$A_T$	Total fractured area
$A_d$	Dynamic fracturing area
$R_d$	Dynamic fracturing radius
$E$	Young's modulus
$E'$	Plane strain Young's modulus
$\nu$	Poisson's ratio
$K_{IC}$	Fracture toughness
$K'$	Reduced fracture toughness
$k$	Dimensionless fracture toughness
$\mu_f$	Viscosity of fracturing fluid
$\mu'$	Dynamic viscosity
$\Phi$	Porosity
$T$	Time
$t_{mk}$	Transition time required for fracture propagation from viscosity dominated to toughness dominated regimes
$t_{om}$	Characteristic time related to fluid lag to toughness dominated regimes
$U$	Compliance of injection system
$\chi$	Time scale ratios of early-time initiation by compressibility of injection system to the late-time propagation under a constant injection $Q_o$
$\Psi$	Time scale ratios of fluid lag to the late-time propagation
$C_o$	Cohesion
$\sigma_T$	Tensile strength
$\sigma_o$	Confining stress or minimum horizontal stress
$\phi$	Porosity
$K$	Permeability
$P_b$	Breakdown pressure
$P_e$	BHP pressure when hydraulic fracture reaches the boundary
$P(t)$	Wellbore pressure during injection time period
$\zeta$	The Fraction of fluid within the hydraulic fracture
$x$	Cartesian coordinates $x$ direction of a penny shaped fracture
$z$	Cartesian coordinates $z$ direction of a penny shaped fracture
$\xi$	A dummy variable possessing same dimension with $x$
$U_z(r)$	The normal displacement of any point on upper part of crack disk

## Reference

- Abé Ha, Keer L, Mura T (1976) Growth rate of a penny-shaped crack in hydraulic fracturing of rocks, 2 Journal of Geophysical Research 81:6292-6298
- Adachi J, Siebrits E, m, Peirce A, Desroches J (2007) Computer simulation of hydraulic fractures International Journal of Rock Mechanics and Mining Sciences 44:739-757
- Advani S, Lee T, Lee J (1990) Three-dimensional modeling of hydraulic fractures in layered media: part I—finite element formulations
- Advani S, Torok J, Lee J, Choudhry S (1987) Explicit time-dependent solutions and numerical evaluations for penny-shaped hydraulic fracture models Journal of Geophysical Research: Solid Earth 92:8049-8055
- Amitrano D (2003) Brittle-ductile transition and associated seismicity: Experimental and numerical studies and relationship with the b value Journal of Geophysical Research: Solid Earth 108

- Batchelor CK, Batchelor G (2000) An introduction to fluid dynamics. Cambridge university press,
- Bunger AP (2005) Near-surface hydraulic fracture. University of Minnesota
- Bunger AP, Detournay E (2007) Early-time solution for a radial hydraulic fracture *Journal of engineering mechanics* 133:534-540
- Bunger AP, Detournay E (2008) Experimental validation of the tip asymptotics for a fluid-driven crack *Journal of the Mechanics and Physics of Solids* 56:3101-3115
- Bunger AP, Gordeliy E, Detournay E (2013) Comparison between laboratory experiments and coupled simulations of saucer-shaped hydraulic fractures in homogeneous brittle-elastic solids *Journal of the Mechanics and Physics of Solids* 61:1636-1654
- Clifton RJ, Abou-Sayed AS A variational approach to the prediction of the three-dimensional geometry of hydraulic fractures. In: SPE/DOE Low Permeability Gas Reservoirs Symposium, 1981. OnePetro,
- Clifton RJ, Wang J-J Adaptive optimal mesh generator for hydraulic fracturing modeling. In: The 32nd US Symposium on Rock Mechanics (USRMS), 1991. OnePetro,
- De Pater C, Cleary M, Quinn T, Barr D, Johnson D, Weijers L (1994a) Experimental verification of dimensional analysis for hydraulic fracturing *SPE Production & Facilities* 9:230-238
- De Pater C, Weijers L, Savic M, Wolf K, Van Den Hoek P, Barr D (1994b) Experimental study of nonlinear effects in hydraulic fracture propagation (includes associated papers 29225 and 29687) *SPE Production & Facilities* 9:239-246
- Detournay E (2004) Propagation regimes of fluid-driven fractures in impermeable rocks *International Journal of Geomechanics* 4:35-45
- England A, Green A Some two-dimensional punch and crack problems in classical elasticity. In: *Mathematical Proceedings of the Cambridge Philosophical Society*, 1963. vol 2. Cambridge University Press, pp 489-500
- Feng R, Zhang Y, Rezagholilou A, Roshan H, Sarmadivaleh M (2020) Brittleness Index: from conventional to hydraulic fracturing energy model *Rock Mechanics and Rock Engineering* 53:739-753
- Fung R, Vilayakumar S, Cormack DE (1987) Calculation of vertical fracture containment in layered formations *SPE formation evaluation* 2:518-522
- Garagash D, Detournay E (2000) The tip region of a fluid-driven fracture in an elastic medium *J Appl Mech* 67:183-192
- Garagash DI (2006) Propagation of a plane-strain hydraulic fracture with a fluid lag: Early-time solution *International journal of solids and structures* 43:5811-5835
- Garagash DI Roughness-dominated hydraulic fracture propagation. In: *EOS Trans. AGU (Fall Meeting Suppl.)*, 2015. vol 52. pp MR41A-2628
- Garagash DI (2019) Cohesive-zone effects in hydraulic fracture propagation *Journal of the Mechanics and Physics of Solids* 133:103727
- Geertsma J, De Klerk F (1969) A rapid method of predicting width and extent of hydraulically induced fractures *Journal of petroleum technology* 21:1571-1581
- Green AE, Zerna W (1992) *Theoretical elasticity*. Courier Corporation,
- Holt RM, Fjær E, Stenebråten JF, Nes O-M (2015) Brittleness of shales: relevance to borehole collapse and hydraulic fracturing *Journal of Petroleum Science and Engineering* 131:200-209
- Huang C, Chen S (2021) Effects of Ductility of Organic-Rich Shale on Hydraulic Fracturing: A Fully Coupled Extended-Finite-Element-Method Analysis Using a Modified Cohesive Zone Model *SPE Journal* 26:591-609
- Lecampion B, Desroches J (2015) Simultaneous initiation and growth of multiple radial hydraulic fractures from a horizontal wellbore *Journal of the Mechanics and Physics of Solids* 82:235-258
- Lecampion B, Desroches J, Jeffrey RG, Bunger AP (2017) Experiments versus theory for the initiation and propagation of radial hydraulic fractures in low-permeability materials *Journal of Geophysical Research: Solid Earth* 122:1239-1263
- Lecampion B, Detournay E (2007) An implicit algorithm for the propagation of a hydraulic fracture with a fluid lag *Computer Methods in Applied Mechanics and Engineering* 196:4863-4880

- Legarth B, Huenges E, Zimmermann G (2005) Hydraulic fracturing in a sedimentary geothermal reservoir: Results and implications *International Journal of Rock Mechanics and Mining Sciences* 42:1028-1041
- Lhomme T (2005) Initiation of hydraulic fractures in natural sandstones
- Liu D (2021) Hydraulic fracture growth in quasi-brittle materials. EPFL,
- Liu D, Lecampion B (2021) Propagation of a plane-strain hydraulic fracture accounting for a rough cohesive zone *Journal of the Mechanics and Physics of Solids* 149:104322
- Nabipour A (2013) Experimental and numerical study of ultrasonic monitoring of hydraulic fracture propagation. Curtin University
- Naceur KB, Thiercelin M, Touboul E (1990) Simulation of fluid flow in hydraulic fracturing: implications for 3D propagation *SPE production engineering* 5:133-141
- Nordgren R (1972) Propagation of a vertical hydraulic fracture *Society of Petroleum Engineers Journal* 12:306-314
- Papanastasiou P, Papamichos E, Atkinson C (2016) On the risk of hydraulic fracturing in CO<sub>2</sub> geological storage *International Journal for Numerical and Analytical Methods in Geomechanics* 40:1472-1484
- Peck D, Wrobel M, Perkowska M, Mishuris G (2018) Fluid velocity based simulation of hydraulic fracture: a penny shaped model—part I: the numerical algorithm *Meccanica* 53:3615-3635
- Perkins T, Kern LR (1961) Widths of hydraulic fractures *Journal of petroleum technology* 13:937-949
- Rodriguez IV, Stanchits S (2017) Spatial and temporal variation of seismic attenuation during hydraulic fracturing of a sandstone block subjected to triaxial stress *Journal of Geophysical Research: Solid Earth* 122:9012-9030
- Rybacki E, Reinicke A, Meier T, Makasi M, Dresen G (2015) What controls the mechanical properties of shale rocks?—Part I: Strength and Young's modulus *Journal of Petroleum Science and Engineering* 135:702-722
- Sarmadivaleh M (2012) Experimental and numerical study of interaction of a pre-existing natural interface and an induced hydraulic fracture. Citeseer,
- Savitski A, Detournay E (2002) Propagation of a penny-shaped fluid-driven fracture in an impermeable rock: asymptotic solutions *International journal of solids and structures* 39:6311-6337
- Shao S, Ranjith P, Wasantha P, Chen B (2015) Experimental and numerical studies on the mechanical behaviour of Australian Strathbogie granite at high temperatures: an application to geothermal energy *Geothermics* 54:96-108
- Shapiro SA (2015) Fluid-induced seismicity. Cambridge University Press,
- Simonson E, Abou-Sayed A, Clifton R (1978) Containment of massive hydraulic fractures *Society of Petroleum Engineers Journal* 18:27-32
- Sneddon I, Elliot H (1946) The opening of a Griffith crack under internal pressure *Quarterly of Applied Mathematics* 4:262-267
- Sneddon IN (1946) The distribution of stress in the neighbourhood of a crack in an elastic solid *Proceedings of the Royal Society of London Series A Mathematical and Physical Sciences* 187:229-260
- Sneddon IN (1995) Fourier transforms. Courier Corporation,
- Valkó P, Economides MJ (1995) Hydraulic fracture mechanics vol 28. Wiley Chichester,
- van Dam DB, Papanastasiou P, De Pater C Impact of rock plasticity on hydraulic fracture propagation and closure. In: *SPE Annual Technical Conference and Exhibition, 2000*. OnePetro,
- Vandamme L, Curran J (1989) A three-dimensional hydraulic fracturing simulator *International Journal for Numerical Methods in Engineering* 28:909-927
- Weinberg RF, Regenauer-Lieb K (2010) Ductile fractures and magma migration from source *Geology* 38:363-366
- Wong T-f, Baud P (2012) The brittle-ductile transition in porous rock: A review *Journal of Structural Geology* 44:25-53
- Zeng L, Reid N, Lu Y, Hossain MM, Saeedi A, Xie Q (2020) Effect of the fluid–shale interaction on salinity: implications for high-salinity flowback water during hydraulic fracturing in shales *Energy & Fuels* 34:3031-3040

Zhel'tov AK 3. Formation of vertical fractures by means of highly viscous liquid. In: 4th world petroleum congress, 1955. OnePetro,

Zhou D, Zhang G, Zhao P, Wang Y, Xu S (2018) Effects of post-instability induced by supercritical CO<sub>2</sub> phase change on fracture dynamic propagation Journal of Petroleum Science and Engineering 162:358-366